LLE Review

Quarterly Report

April–June 1985

UR
LLE

LLE Review

Quarterly Report

Editor: S. Skupsky
(716) 275-3951

April–June 1985

UR
LLE

IN BRIEF

This volume of the LLE Review contains articles on the fully UV-converted OMEGA laser system, mass-ablation rate experiments, reactor-size target designs, plasma processes in the target corona, degradation in optical performance of dielectric thin films, and the National Laser Users Facility activities for April–June 1985.

The following are some highlights of the work described in this issue:

- All 24 beams of the OMEGA laser system have been converted from IR (1054 nm) to UV (351 nm). Previous 6- and 12-beam UV experiments on heat transport, implosion, and x-ray physics are being re-examined at the higher level of uniformity possible with 24 beams, and with an increased number of diagnostic instruments. The system has operated with up to 40 shots per week, and up to 2.4 kJ on target. During system checkout, a record neutron yield of 2×10^{11} was obtained.

- Work is nearly complete for using GDL as a 25th beam of OMEGA to create an x-ray backlighting source for OMEGA experiments.

- The UV beam quality of OMEGA is being quantitatively analyzed to bring the on-target irradiation uniformity to the level required for high-density experiments. Some sources of beam imperfections have been identified and a program for beam improvement is being implemented.

- Previous UV experiments on time-resolved heat transport using 6 and 12 beams have been analyzed. Some discrepancies between theoretical modeling and experiment have been found, but they were consistent with the poor irradiation uniformity inherent in the 6- and 12-beam geometry. These experiments are being repeated with 24 beams.

- The effects of irradiation nonuniformity on direct-drive, reactor-size targets have been examined using two-dimensional hydrodynamic simulations. The degradation in target gain with increased nonuniformity has been calculated for long-wavelength nonuniformities (spherical harmonic modes $\ell \leq 8$).

- A new model for examining stimulated Raman scattering (SRS) in the plasma atmosphere has been developed, and a steady-state analytic solution of the process is obtained.

- Thin films, which might be used in excimer lasers, can be surface damaged by exposure to electrons and ions in the laser medium of the laser. A sensitive technique (photothermal displacement spectroscopy) is used for measuring the degradation in optical performance of the thin film.

CONTENTS

Patrick W. McKenty, a scientist in the Theory and Computation Group, is examining results from hydrodynamic simulations of high-compression, laser-driven implosions.

Section 1
LASER SYSTEM REPORT

1.A GDL Facility Report

GDL has been shut down for the complete replacement of the front end with the actively mode-locked, Q-switched (AMQ) oscillator and predriver. Work has continued throughout this period on activation and alignment of the oscillator, a refurbishment of the active mirror system, and complete system realignment. A portion of the GDL downtime was caused by construction efforts to cut holes for the 25th-beam project and installation of the periscope. (The beam will be used for creating an x-ray backlighting source for OMEGA experiments.) Plans call for activation of the system to support NLUF experiments during July.

1.B   OMEGA Facility Report

The OMEGA laser system has operated this entire quarter as a fully ultraviolet, 24-beam irradiation facility. Initial experiments were performed to examine neutron yield, thermal transport, and uniformity of irradiation. During system checkout, a record neutron yield of 2×10^{11} was obtained. Collaborative experiments with other laboratories (Los Alamos National Laboratory, University of Florida, and University of Maryland), through the National Laser Users Facility, examined different aspects of x-ray physics.

In parallel with the experiments, the newly UV-converted system was adjusted for energy balance between beams, beam alignment, and energy output. Energies on target were typically greater than 2 kJ, with a maximum of 2.42 kJ. Energy variation among the beams was at the 5% level, with the smallest variation 3.4%. At times, a multishift operation was used to attain a shot rate of 30 to 40 per week in support of the thermal transport studies and the x-ray conversion studies.

Many new diagnostic instruments were activated during this period, including four independent x-ray streak cameras. Progress was made toward successfully activating a time fiducial on the elliptical crystal streak spectrograph using a portion of the driver-line output, which was transported to the target chamber ahead of the main beams, converted to the fourth harmonic (175 nm), and directed to the camera via fiber optics. In collaboration with Los Alamos National Laboratory (LANL), progress was also made to activate the miniflex x-ray diode system. An experimental systems operator was added to streamline experimental operation of the system; this led to a substantial increase in the shot rate.

The facility work was completed for the 25th-beam project, and the periscope to elevate the GDL output beam to the OMEGA target bay level was installed. Installation of the 25th beam is planned for July and August. The AMQ oscillator project is on schedule for OMEGA installation in late July.

A summary of OMEGA operations this quarter follows:

Driver Shots	43	(11%)
Beamline Test Shots	7	(2%)
Software Tests and Failures	43	(11%)
Target Shots	294	(76%)
TOTAL	387	(100%)

1.C OMEGA Uniformity Program

It is expected that fluctuations in laser intensity over the target surface must be kept below a few percent to drive high-density implosions. Although various theoretical[1,2] and experimental[3,4] aspects of irradiation uniformity have been under investigation for several years, the need for high-quality laser-beam profiles has not been a crucial issue, as high-density implosions have not been possible. The 24-beam IR implosion experiments[3] were relatively insensitive to illumination nonuniformity due to the smoothing action of the copious amounts of fast electrons from resonance absorption, but these electrons also preheated the target, preventing high compression. The 6-beam UV implosion experiments[4] were free of fast electrons, but they were dominated by the large nonuniformity inherent in the 6-beam geometry. However, the 24-beam UV irradiation now available on OMEGA removes a great part of this inherent geometrical contribution to nonuniformity, and opens the possibility for high-density ablative implosions if good beam quality can be achieved. Smooth beam profiles are possible and have been obtained on the GDL system.[2] There is now a strongly increased effort to quantitatively assess and improve the beam quality on OMEGA.

In order to translate the hydrodynamic uniformity requirements into laser beam quality requirements, we have developed a three-dimensional (3-D) beam superposition code. This code permits the input of two-dimensional (2-D), digitized images for each of the 24 beams of OMEGA, or for any arbitrary profile. Studies were performed to assess the sensitivity of target irradiation to particular types of illumination nonuniformity, such as noncircularity, irregularities in beam profiles, target misalignment, beam energy imbalance, and mispointing of beams on target. The output of this code yields overall rms fluctuations as well as the amplitudes of a spherical harmonic decomposition of the nonuniformity. The results can be summarized as follows: beam energy imbalance, mispointing, and noncircular beams all contribute to ℓ-modes below $\ell = 4$. Beam profile fluctuations, on the other hand, predominantly contribute to modes with $\ell \geq 8$. Purely geometrical effects related to beam overlap for the 24-beam OMEGA illumination configuration predominantly produce modes with $\ell = 8$–12, even for perfect beams.

Experimentally, the capability of measuring individual beam energies to an accuracy of 1% has been developed, and beam energy balance in the 2 to 3% range is now achievable. With refinements, a 1% beam energy balance can be envisaged. Similarly, mispointing on target can easily be kept within 10 to 20 μrad, which is considered adequate for high-density implosions. The remaining laser beam characteristic enhancing low-order ℓ-modes, the beam circularity, relates mostly to laser alignment. As such, appropriate alignment procedures should bring this problem well within tolerable limits.

With a number of uniformity issues removed, the main thrust of the uniformity program at LLE involves assessment and improvement of the individual laser beam profiles with their superposed, more or less random intensity fluctuations. The theoretical requirement for beam quality is to approach a quadratic intensity profile with intensity fluctuations not exceeding 20% peak to valley.[2]

(a)

Array
Photograph

(b) Density Histogram

Area (arbitrary units)

Density

(c) D-Log I

Density

Log I

(d) Intensity Contour Plot

mm

50%
75%
25%
1%
95%

Distance (mm)

(e) Intensity Histograms (ETP)

$dE/dl, \int_0^l (dE/dl)dl$

$\int_0^l (dE/dl)dl$

dE/dl

Intensity (MW/cm^2)
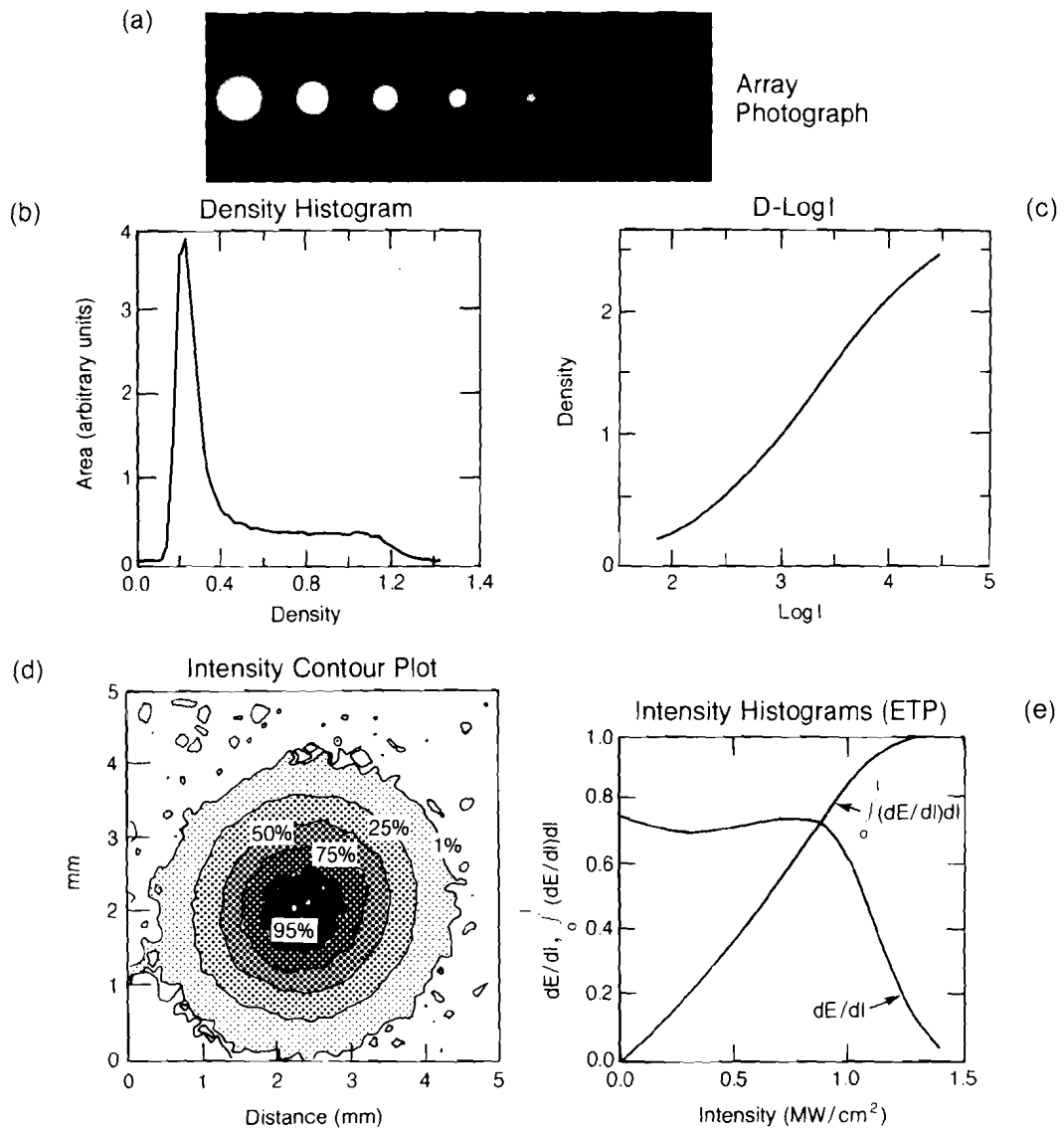
E3487

Fig. 23.1

Image processing. (a) Array photograph with successive images attenuated by factors of 2. (b) Density histogram of one of the images. Using two density histograms of the images in (a) we obtain film intensity response curves (D-logI) shown in (c). An intensity contour plot of an expanded oscillator beam is shown in (d). The corresponding intensity histogram (dE/dl vs I) as well as its integrated counterpart are shown in (e). The flat histogram is close to the rectangular histogram expected for a Gaussian beam.

In order to assess the beam quality on target accurately, we have re-examined laser performance by photographing the laser beams in the near field (at the output of the laser system), as well as in the equivalent target plane of an auxiliary focusing lens, with a much longer focal length than the actual OMEGA focusing lenses. This arrangement[5] leads to satisfactory mapping of the on-target intensity distribution if the actual focusing lenses are close to diffraction limited. The quantitative analysis of these photographs involves a recently acquired Perkin-Elmer 2-D microdensitometer along with computerized image analysis codes. This analysis includes a D-logI intensity response conversion, contour plotting, and intensity histograms. Figure 23.1 illustrates the process, from taking array photographs of an image, to density histograms, intensity response curves (D-logI), contour plots, and intensity histograms. While size and symmetry properties can be obtained conveniently from contour plots, the intensity histogram (dE/dI vs I) shown in Fig. 23.1(e) frequently yields very useful data for the interpretation of laser-fusion experiments (average and peak intensities, etc.) as well as for rapid evaluation of the on-target irradiation nonuniformity. Since Fig. 23.1 is an image of the oscillator output, it approximates very closely a Gaussian profile, for which the intensity histogram (dE/dI vs I) is a rectangle.

The intensity distribution in the target plane (quasi far field) depends on the intensity and phase distribution of the beam incident on the focusing optics. A smooth near-field beam intensity distribution, as shown in Fig. 23.2, is therefore a requirement for a smooth equivalent-target-plane (ETP) intensity distribution. However, the detailed phase

$\lambda_L = 351$ nm, 700 ps

Distance (cm)
(resolution: 1.6 mm)
E3692
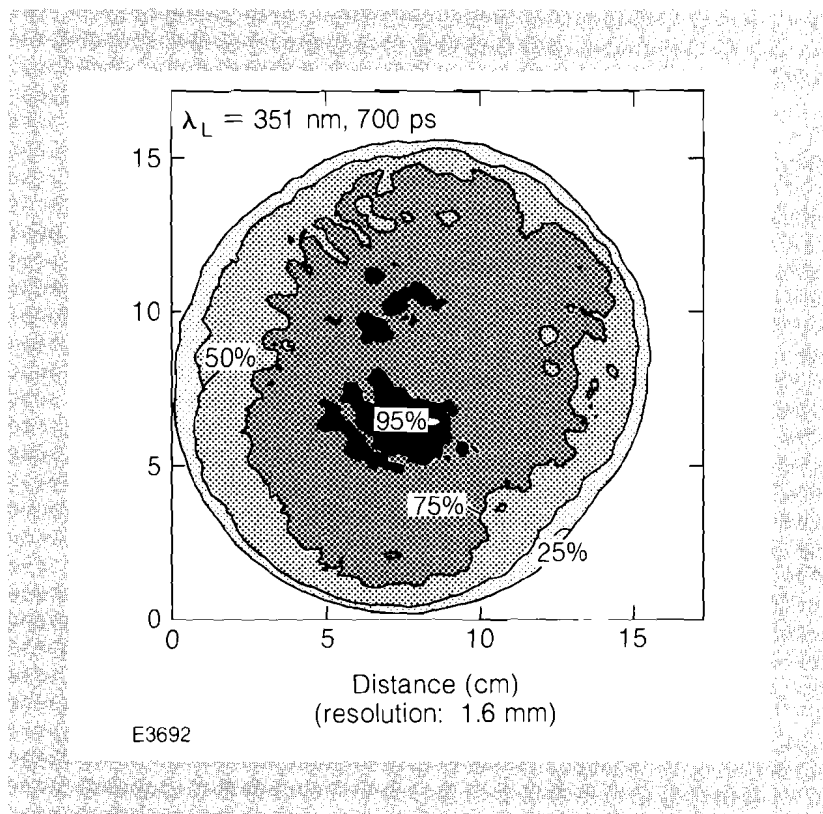
Fig. 23.2
Intensity contour plot of a UV near-field image at the output of the up-conversion crystal in OMEGA.

front distribution of this beam is very difficult to measure, and frequently the ETP distribution is taken instead. Figure 23.3 shows two such ETP contour plots with their corresponding intensity histograms. The effect of air turbulence is shown: one image is under normal operating conditions and the other has reduced turbulence. While the median intensity in the two images is roughly equal, the ratio of maximum to median intensity is approximately two times larger for the beam suffering from strong air turbulence. The 3-D superposition code (using the same beam profiles for all 24 beams of OMEGA) also showed that the rms nonuniformity for the poorer beam profile resulted in an rms nonuniformity over the target surface of roughly twice that for the case with reduced turbulence ($\sigma_{rms} \approx$ 30% and 15%, respectively).

OMEGA, λ_L = 351 nm, (1ns, 100 J nominal)

Reduced Turbulence   Strong Turbulence

Distance in Target Plane (μm), 10-μm Spatial Resolution

Intensity Histograms

	10964	10966	Gaussian
$\dfrac{I_{100}}{I_{50}}$	3.2	6.2	2
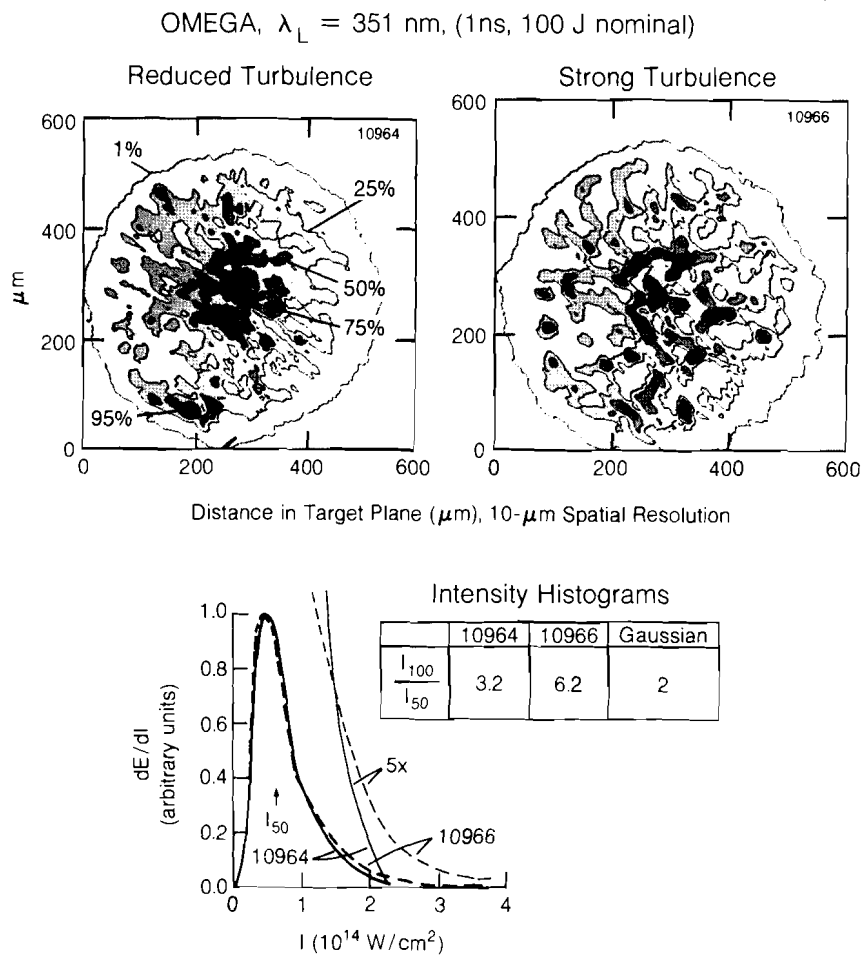
E3484

Fig. 23.3
Equivalent-target-plane intensity distributions for one of the OMEGA UV beams with strong and reduced air turbulence. The effect of reducing air turbulence is particularly evident in the histograms, where it leads to a peak-to-median intensity ratio that is half as large as the one for strong turbulence. The effect of increased turbulence manifests itself in increased intensity gradients and patchy contour plots.

Analysis of the up-conversion crystals[6] also showed that many of them contribute significantly to the phase-front distortions on the beams, particularly in the form of small-scale phase gradients. Figure 23.4 is a demonstration of how different crystals affect the ETP intensity distribution of an auxiliary 351-nm alignment beam [Fig. 23.4(a)]. The best up-conversion cell available at LLE hardly changes the ETP contour plot or intensity histogram over that of the undisturbed alignment beam [compare Figs. 23.4(a) and 23.4(b)], while the worst crystal assembly leads to dramatic changes [Figs. 23.4(c) and 23.4(d)]. In particular, the intensity histogram shows a maximum intensity that is twice that of the ETP of the undisturbed alignment beam. Here, too, the 3-D superposition code showed that the rms intensity fluctuations of the 24 beams of OMEGA on the target are approximately two times worse
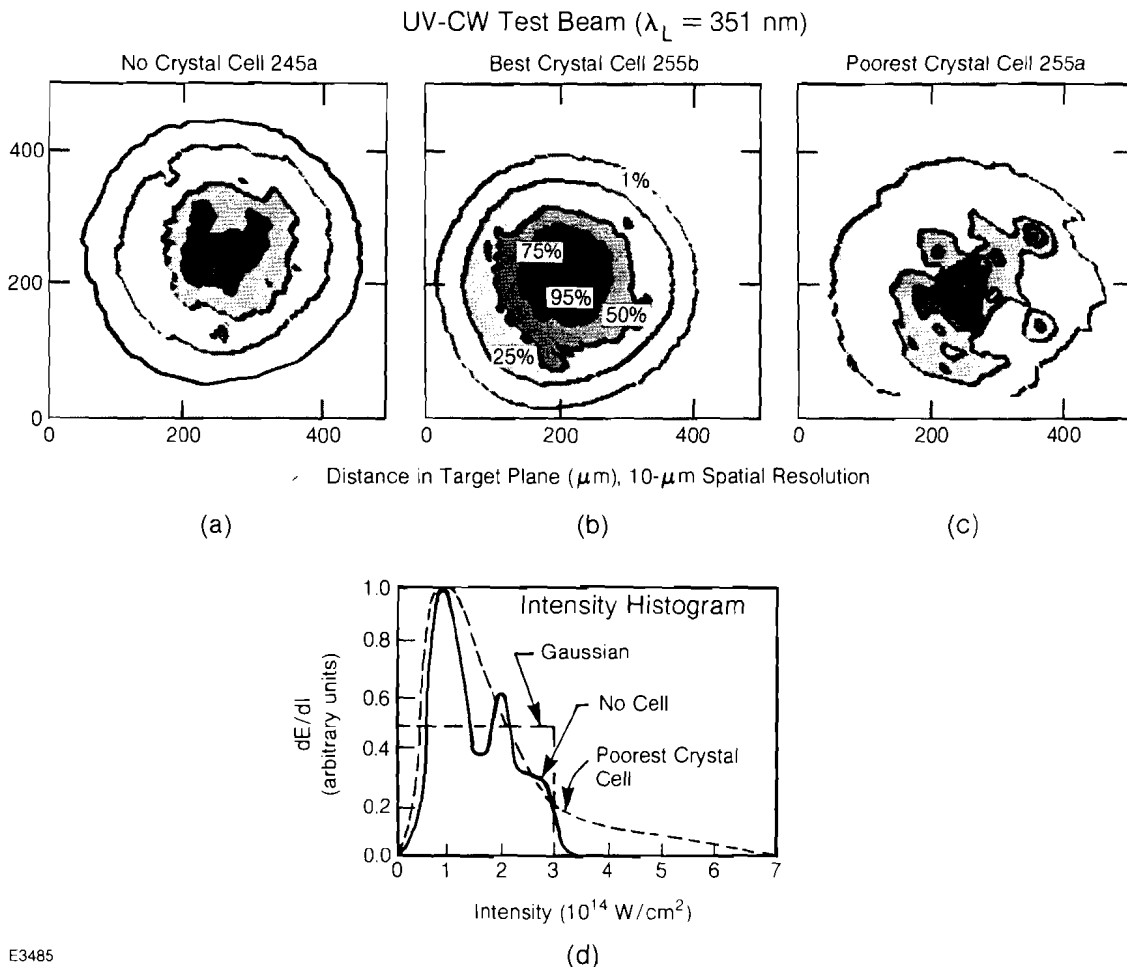
Fig. 23.4
Effect of different up-conversion crystal cells on equivalent-target-plane intensity distributions. The ETP contour plot of an auxiliary cw UV alignment beam is shown in (a). The best LLE up-conversion cell hardly affects this distribution (b), while the worst cell strongly distorts the distribution (c) and increases the peak-to-median intensity ratio (d) by a factor of 2.

when the intensity distribution of Fig. 23.4(c) was used, as compared to Fig. 23.4(a) ($\sigma_{rms} \gtrsim$ 10% and 5%, respectively).

The results shown above suggest a near-term uniformity program that concentrates on problems related to air turbulence, beam propagation, and crystal quality. The longer-term program focuses on the intrinsic laser performance and its improvements. This includes the implementation on OMEGA of the recently developed holographic method for analyzing the phase distribution in the near field of the laser output.[7] In addition, a low-level effort is under way to study the feasibility of using random phase plates[8] or their equivalent to increase the average on-target illumination uniformity.

ACKNOWLEDGMENT

REFERENCES

1. "Short-Wavelength, Single-Shell, Direct-Drive Pellet Designs," LLE Review (this issue).

2. S. Skupsky and K. Lee, *J. Appl. Phys.* **54**, 3662 (1983); LLE Review **19**, 120 (1984).

3. M. C. Richardson, T. R. Boehly, B. A. Brinker, T. C. Bristow, R. S. Craxton, J. A. Delettrez, G. Enright, A. Entenberg, W. Friedman, L. M. Goldman, J. Hoose, R. J. Hutchison, L. Iwan, S. Kacenjar, K. Lee, S. A. Letzring, L. D. Lund, R. S. Marjoribanks, R. L. McCrory, J. M. Miller, J. Rizzo, W. D. Seka, S. Skupsky, J. M. Soures, C. P. Verdon, D. M. Villeneuve, E. A. Williams, and B. Yaakobi, in *Laser Interaction and Related Plasma Phenomena*, edited by H. Hora and G. K. Miley (Plenum, New York, 1984), Vol. 6, p. 903; M. C. Richardson *et al.*, in *Plasma Physics and Controlled Nuclear Fusion Research 1982* (IAEA, Vienna, 1983), p. 477; LLE Review **10**, 11 (1982).

4. LLE Review **20**, 150 (1984).

5. LLE Review **17**, 7 (1984).

6. R. P. Bossert, S. D. Jacobs, and L. D. Lund, in NBS Special Publication 669: *Proceedings of the 14th Annual Symposium on Optical Materials for High Power Lasers: 1982*, edited by A. Guenther, H. Bennett, B. Newman, and D. Milam (NBS, Colorado, 1984), pp. 118–129.

7. LLE Review **18**, 61 (1984).

8. Y. Kato *et al.*, *Phys. Rev. Lett.* **53**, 1057 (1984).

1.D   Synchronization of Two Actively Mode-Locked and Actively Q-Switched Oscillators

For the recently upgraded GDL laser system[1] to be used as a synchronized x-ray backlighting source for laser-fusion experiments on the 24-beam OMEGA system, it has become necessary to modify the present active-passive mode-locked oscillators[2] into synchronizable, actively mode-locked and Q-switched oscillators (AMQO). The oscillator is based on a Lawrence Livermore National Laboratory (LLNL) design;[3] the opto-mechanical elements of this oscillator, however, were completely redesigned to meet the particular needs of LLE.[4,5] The application of the LLNL approach to synchronization of multiple oscillators was not straightforward, as the GDL and OMEGA oscillators are physically separated by ≈ 75 m. In addition, the original rf electronics proved too sensitive to electromagnetic interference (EMI) to be operated reliably in our laboratory environment. Because of these factors, it became necessary to redesign this part of the oscillator.

In this article we describe the basic principles,[5] design criteria, and performance characteristics of the new rf electronics for the AMQO. Also discussed are novel diagnostics and synchronization data. The opto-mechanical design is given elsewhere.[4,5]

AMQO RF Electronics

In the new design all low-level rf analog signal processing was replaced by CMOS integrated circuit technology because of its high noise immunity. Furthermore, advanced Schottky TTL was used where very high speed was required. Careful design, layout, grounding, and shielding practices make this new design very resistant to EMI.

There is one master rf oscillator, which provides the synchronization for all the oscillators and for a number of relevant timing signals. The rf synchronization is designed around a stable quartz crystal oscillator operating at 66 MHz; the repetition rate signal is obtained from amplitude modulation of the rf. Each one of the separate remote rf control and timing units then detects the leading edge of this amplitude modulation. All other timing signals are generated internally in the remote-control unit, using the phase of the 66-MHz rf or the leading edge of the modulated rf.

One of the remote-control units is designated the master unit, to which all others are slaved. This is a result of a peculiarity of the design, since the total delay of the q-switch pulse with respect to the repetition rate pulse is of the order of milliseconds and its adjustability should be of the order of nanoseconds. (This nanosecond precision proved difficult and a resolution of ± 1 μs was chosen instead.) However, if each remote unit were to generate its own q-switch pulse, the resulting optical pulse trains would also be afflicted by a microsecond jitter, making oscillator synchronization impossible. Thus, the q-switch pulse generated by the master control unit is routed to the slave units, triggering the q-switch pulses in those units with less than 50-ps jitter. The jitter between the actual optical pulses (from different

oscillators) in the AMQO pulse train primarily depends on the short-term (ms) phase stability of the rf to the acousto-optic mode-locker. This short-term frequency stability has been measured to be approximately 10 ppm/ms. In addition, the remote control units contain three independent high-precision delay units—for triggering, for instance, the single-pulse switch-out electronics (Pockels cell drivers) or streak cameras. These delay generators have a least-count resolution of 16 ns and a measured jitter of 30–40 ps between any two delay generators within a control unit as well as between control units.

The concept of AMQO's separated physically by long distances and driven by remote rf control units with their proper rf amplifiers requires extraordinary amplitude and phase stability of the rf link between master rf oscillator and control units. To achieve a 30-ps optical pulse jitter between two different AMQO's, we require a phase stability of 1 mrad and an amplitude stability of 0.1%. Given the long distances and the adverse environment with several °C temperature fluctuations, such stability can only be achieved through the use of very high quality cable[6] with phase stability of 2 to 3 ppm/°C instead of the 200 to 300 ppm/°C for usual coax cable. (The latter would lead to 90 ps/°C optical pulse jitter.) This special cable also has very low loss characteristics (1.2 db/100 ft at 66 MHz), thus satisfying both phase and amplitude stability requirements for the transmission of the rf signal to the remote-control units.

Another major change was made in the design of the flash-lamp driver power supply. This power supply furnishes starting pulse, simmer and boost simmer current pulses, as well as the main lamp discharge pulse. The original design was limited to a peak current of 40 A and required water cooling of more than 40 high-power transistors. This power supply was redesigned using new convection-cooled power transistor modules instead of the water-cooled transistor bank. This also allowed delivery of up to 60-A peak discharge current in a flat-top pulse. The overall reliability of the system was also significantly increased by these design changes.

AMQO Performance

In order to better understand the data below, a brief description of the AMQO is necessary. Figure 23.5 shows the mechanical layout of the oscillator, whose overall length is $\approx$ 1.2 m. The laser host is Nd:phosphate glass (KIGRE Q-100, 4-mm diam $\times$ 100-mm length). The acousto-optic modulators are fabricated in-house[4] and operate at 66 MHz (mode-locker, AOML) and 33 MHz (q-switch, AOQ). A typical pulse train, including prelasing, is shown in Fig. 23.6. Due to the relatively low gain and slope efficiency of the glass laser host as compared to Nd:YLF or Nd:YAG, the output energy of the oscillator is limited to 40 – 70 μJ per single pulse. However, the output beam has a high-quality intensity distribution (see beam-intensity contour plot in Fig. 23.7) and contrast[7] ($\gtrsim 10^5$).

The repetition rate for these oscillators is limited to 0.5 Hz due to the poor thermal conductivity of the glass laser host. (In fact, for OMEGA and GDL, the oscillators are expected to be operating at 0.1 Hz.)
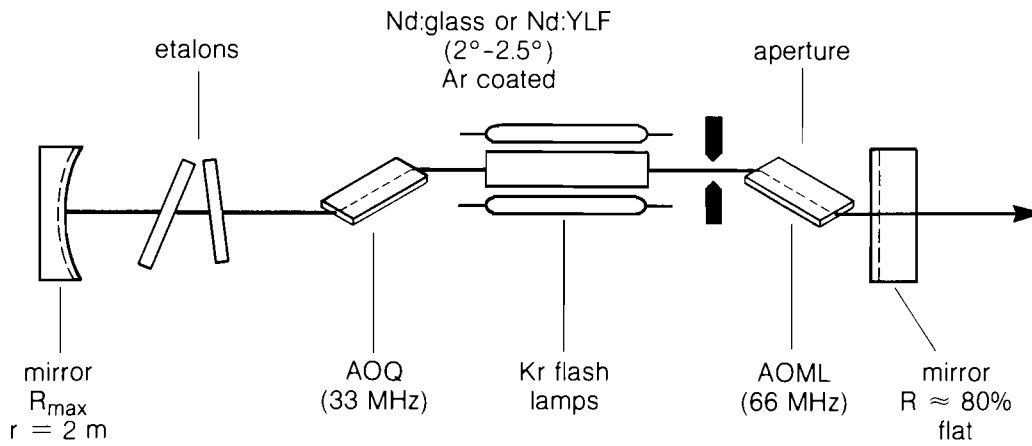
Fig. 23.5
Schematic layout of the major optical components of the AMQO. (AOML: acousto-optic mode-locker; AOQ: acousto-optic q-switch).

(a) Prelase Phase
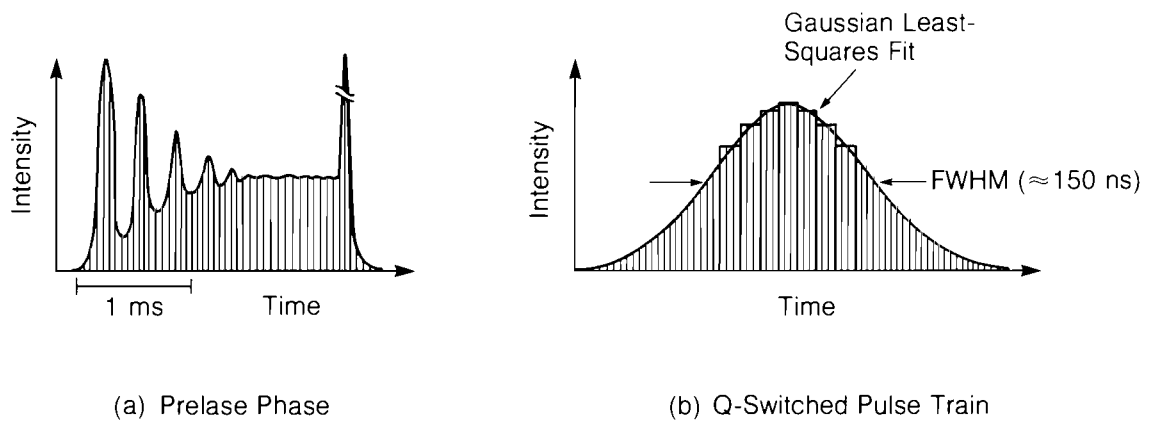
(b) Q-Switched Pulse Train

Fig. 23.6
Typical pulse train obtained with an AMQO. (a) The prelase phase, with its characteristic relaxation oscillations. (b) The q-switched pulse train along with the computer characterization.
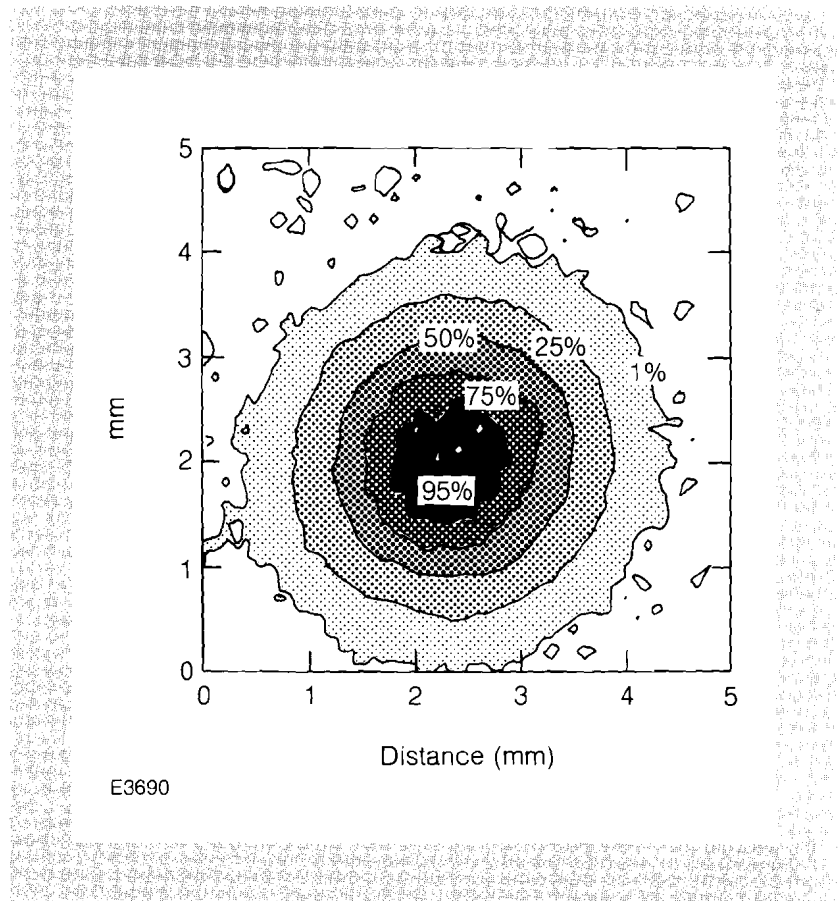
Fig. 23.7
Intensity contour plot of the AMQO output beam with glass laser host. We note the highly symmetric profile, which has been shown to be Gaussian over more than two decades using a diode array.

To facilitate AMQO performance evaluation we have developed a novel diagnostic method using a photodiode and a multichannel-gated integrated A/D converter (LeCroy model 2249W), which is coupled to a PDP11/2 computer. The block diagram for this setup is shown in Fig. 23.8. A small part of the oscillator output is incident on a fast photodiode (HP4202, $t_r \geq 1$ ns); it is split seven ways, with cable delays set up between the 50-Ω splitters in such a way that a "coarse" image of the pulse train can be reconstructed by the computer from the gated A/D signals (Fig. 23.9). Each pulse train is analyzed by fitting a Gaussian envelope using a least-squares fitting routine, which yields a measure of the pulse energy at the peak of the train, the FWHM of the train, and the position of the peak of the train. After averaging, the standard deviation of the peak position yields the jitter of the pulse train envelope with respect to the q-switch initiation signal. This diagnostic has proven operationally very useful since it rapidly signals any malfunctioning of the oscillator.

Typical fluctuations of the peak and the FWHM of the pulse train envelope range between 1% and 3% while the jitter of the pulse train maximum is 15 – 20 ns for a FWHM of 350 ns. We note that the length of the pulse train depends on such parameters as the pump power, the q-switch level, and the laser host; it is therefore very different for different laser materials such as glass, YLF, or YAG.
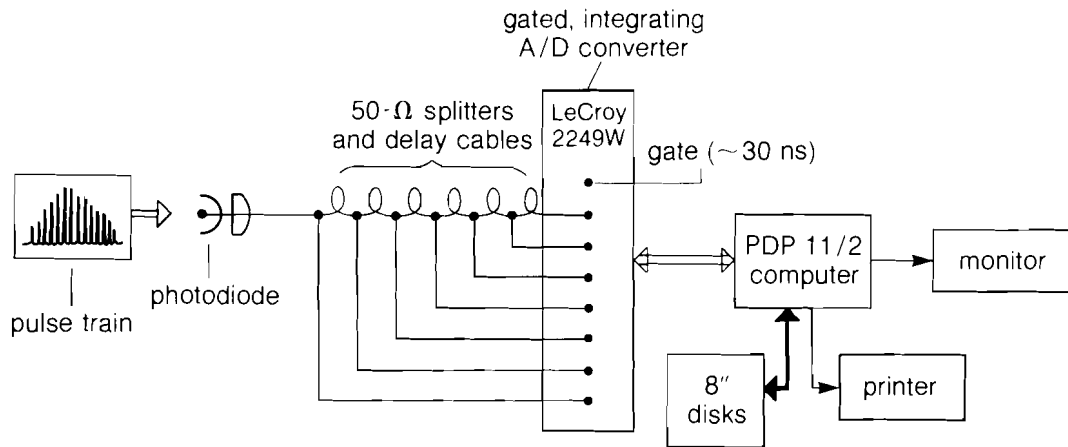
E3673

Fig. 23.8
Block diagram for computerized pulse train monitor. The pulse train seen by the diode is split, delayed, and integrated by a LeCroy-2249W-gated, integrating analog-to-digital converter.

Fig. 23.9
Typical display obtained with computerized pulse train monitor. The standard deviation of the position of the pulse train maximum is also the jitter of the pulse train envelope. The statistics shown here are for typical performance of well aligned AMQO. The averages and standard deviation are obtained over 50 successive shots.
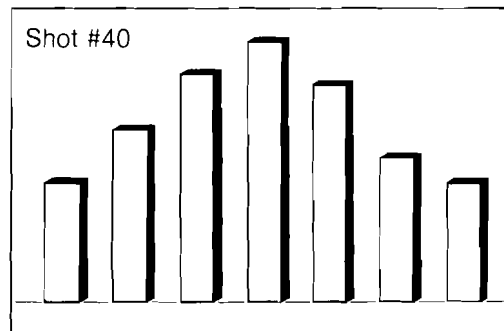
	last shot	average	std. deviation
Single pulse	50 μJ	45 μJ	1%
Train energy	750 μJ	728 μJ	1%
FWHM	358 ns	348 ns	5%
Max. position	400 ns	415 ns	5 ns

E3674

113

AMQO Synchronization

Synchronizing two separate AMQO's requires not only rf synchronization (pulse-to-pulse synchronization) but also pulse train envelope synchronization, to at least 10% of the FWHM of the pulse train. The pulse train monitor described above permits verification and quantitative measurement of the envelope synchronization. For the pulse-to-pulse synchronization we used a streak camera in a novel configuration.

The OMEGA and GDL oscillators typically operate in very different pulse-length regimes (OMEGA: $t_p \approx 1$ ns; GDL: $t_p \approx 0.1$ ns) for experimental reasons related to laser fusion and x-ray backlighting. This allows an experimental setup and pulse display on a picosecond streak camera as shown in Fig. 23.10, where A and B are the first and second pulses of the pulse train generated by the 95% etalon (pulse stacker) in the diagnostic beam from the short-pulse oscillator.

E3675

(a)

(b)
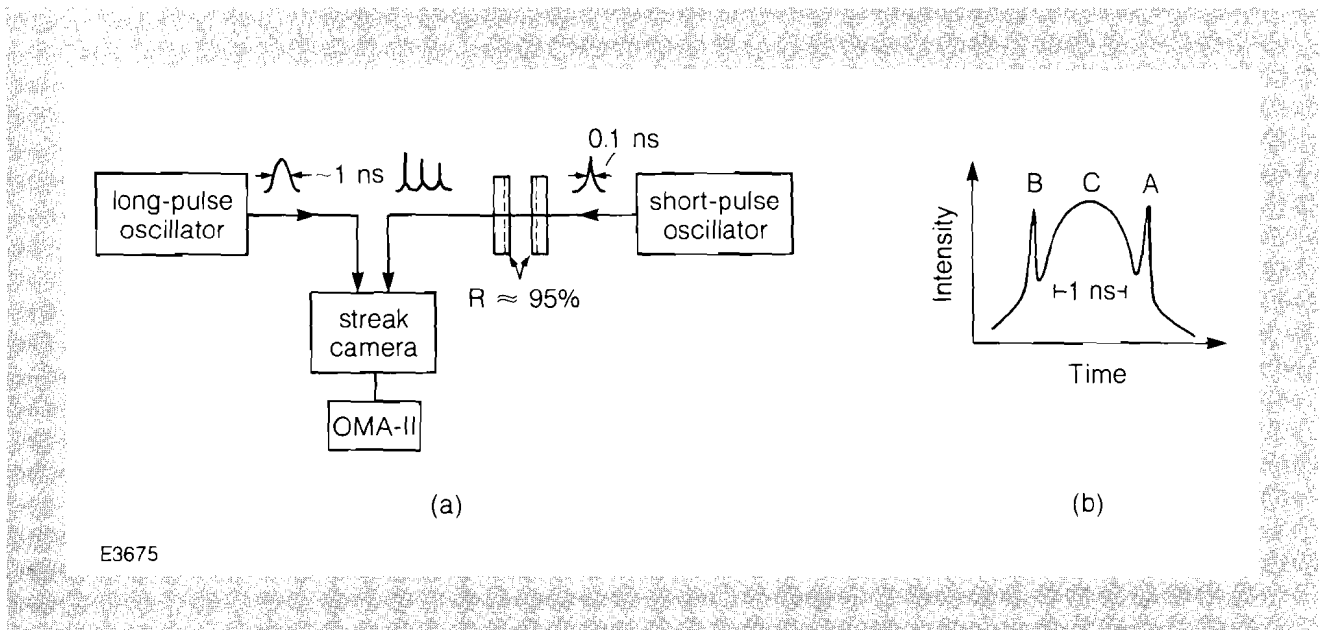
Fig. 23.10
(a) Schematic diagram for streak camera setup for jitter measurements from two oscillators with vastly different pulse durations. The OMA-II is a commercial, optical multichannel analyzer (EG&G-PAR).
(b) Schematic display of Gaussian pulses for optimum jitter measurements. The short pulses are positioned close to the half-intensity points of the long pulse.

The pulses also provide autocalibration of the time axis of the streak record. The pulse from the long-pulse oscillator (C) is timed to fall in between A and B. The synchronization jitter between the two laser pulses can then be obtained from the position of the three pulses on successive shots. Alternatively, measuring the ratio of the peaks A and B also allows determination of the synchronization jitter since the placement of A and B at about the half-intensity points of C renders this ratio very sensitive to the jitter, as seen in Fig. 23.11. An analysis of a representative series of shots, using the two methods just described, yielded a pulse-to-pulse jitter for the long-pulse and short-pulse oscillators of approximately 22 and 29 ps.
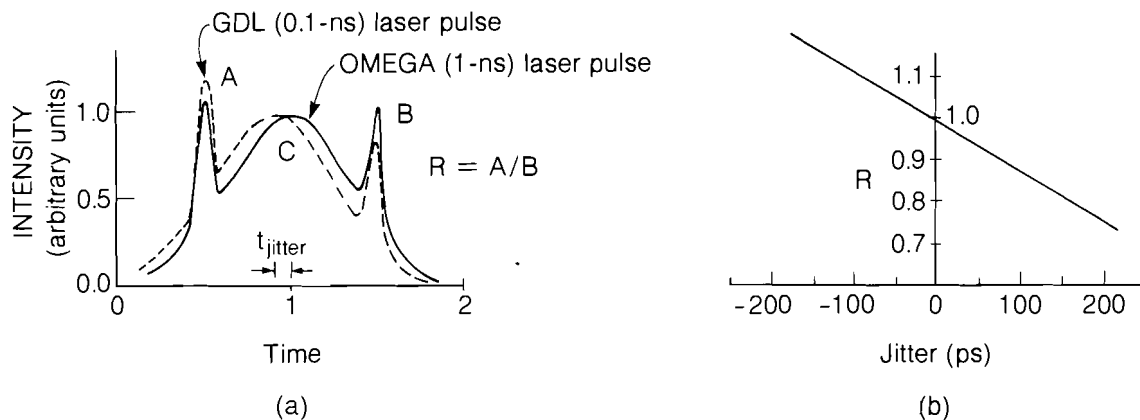
E3450

Fig. 23.11
(a) Display of actual streak record corresponding to the setup shown in Fig. 23.10.
(b) Dependence of the ratio R = A/B, where A and B are the peak intensities of the two short pulses in (a). The straight line in (b) varies only slightly in slope for varying relative intensities between the short and long pulse or their half-widths.

The 20- to 30-ps jitter data between the two AMQO pulses are sufficient for synchronized OMEGA/GDL experiments. So far, we have not determined the source of this jitter or its ultimate limit. However, the present values appear to be close to the instrumental limit for measuring the relative timing of two pulses of vastly different pulse durations. On the other hand, mechanical vibrations of some AOML components at or below the kHz regime at amplitudes around 0.5 μm could also account for the 20- to 30-ps jitter. Our present experimental setup is not optimal in this regard and could conceivably contribute significantly to the present jitter measurements.

ACKNOWLEDGMENT

REFERENCES

1. LLE Review 21, 1 (1984).

2. W. Seka and J. Bunkenburg, J. Appl. Phys. 49, 2277 (1978).

3. D. J. Kuizenga, IEEE J. Quantum Electron. 17, 1694 (1981).

4. G. F. Albrecht, L. Lund, and D. Smith, Appl. Opt. 22, 1276 (1983).

5. G. F. Albrecht, M. Grueneisen, and D. Smith, accepted for publication in IEEE J. Quantum Electron. (1985).

6. Andrew 35422-9 phase stabilized air dielectric HELIX cable.

7. G. F. Albrecht, Opt. Commun. 41, 287 (1982).

Section 2
PROGRESS IN LASER FUSION

2.A Temporal Dependence of the Mass-Ablation Rate in UV-Laser-Irradiated Spherical Targets

Thermal transport in spherical targets, uniformly irradiated with multiple, nanosecond-duration laser beams, has been a topic of much theoretical[1] and experimental interest.[2-6] Understanding thermal transport is important in that it directly affects laser-induced ablation processes, which drive the implosion of direct-drive laser-fusion targets. The direct measurement of the transport of thermal energy from the absorption region to the ablation surface is not possible. However, the mass-ablation rate, $\dot{m}$ (gm/cm²-s), which is very closely related to thermal transport and is a measure of the depth of material penetrated by the heat front during the laser pulse, can be measured through a variety of diagnostics, such as plasma velocity and x-ray spectroscopic techniques.

There is a growing body of experimental measurements of $\dot{m}$, some of which appear to suggest that the transport of thermal energy is inhibited. Computer simulations of these experiments place an upper limit on the heat flux q,[7] such that $q = \min (q_{c1}, f\ q_{fs})$, where q_{c1} is the classical value, q_{fs} is the free-streaming limit, and f is referred to as the flux limiter. Experiments in spherical geometry have inferred various levels of flux inhibition. With $\lambda = 1.05$-μm laser irradiation,[2-5] values range from as low as $f = 0.06$ to values in excess of the free-streaming limit. In Ref. 4, a low-temperature foot on the heat front was observed that cannot be explained with a simple flux-limited inhibition model. At $\lambda = 0.53\ \mu$m,[2] a flux limiter of $f > 0.1$ has been inferred. In experiments at $\lambda = 0.35\ \mu$m,[6] the charge collector versus time-integrated x-ray spectroscopy measurements show markedly different values of $\dot{m}$ and of its scaling with absorbed intensity I_A.

This broad range of inferred flux limiters from apparently similar experiments is difficult to reconcile. The inconsistency could be due to differences in experimental parameters, such as laser pulse shape and irradiation geometry and uniformity. Other factors, such as the shorter scale lengths on smaller targets and the onset of resonant absorption at higher intensities, will also affect thermal transport. Further, important consideration must be given to the influence of time-dependent effects. The time dependence of the mass-ablation rate and its scaling with absorbed intensity have been examined here using the first 6 and 12 UV-converted beams of OMEGA, and the results have been compared with computer simulations.

Computer Simulations of $\dot{m}$

In Fig. 23.12, we present the instantaneous mass-ablation rate during a pulse as a function of the instantaneous absorbed intensity (referenced to the original target diameter) as calculated by the one-dimensional (1-D) Lagrangian code *LILAC*.[8] Laser parameters were λ = 0.351 μm, power = 2.5 TW, Gaussian pulse shape with a 600-ps FWHM, and tangential focusing conditions, producing an incident intensity I_0 = 5×10^{14} W/cm^2 on a 404-μm-diameter target. Code simulations include ray tracing using the azimuthally averaged laser spatial profile, radiation transport with LTE opacities, and heat flux as the harmonic mean of q_{cl} and fq_{fs}. Simulations were run for a variety of flux limiters ranging from f = 0.02 to f = 0.4. The case for f = 0.1 is
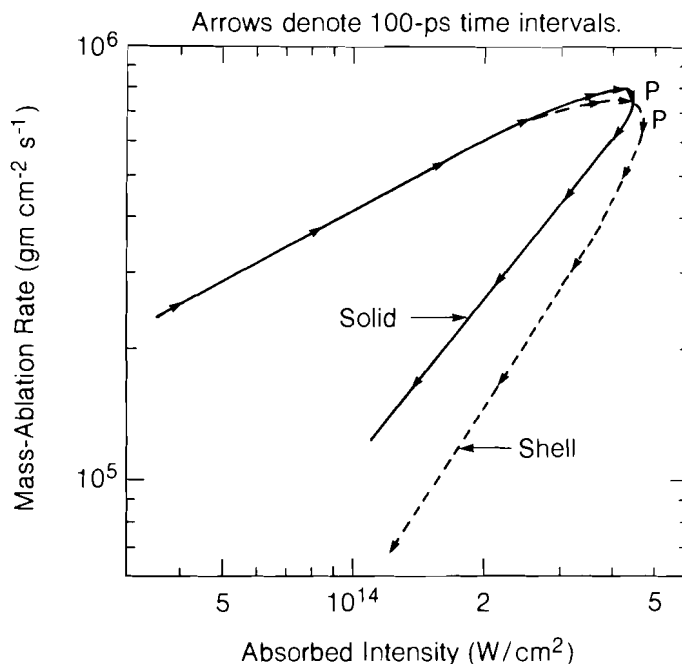
Fig. 23.12
LILAC *simulation for the instantaneous mass-ablation rate [from Eq. (1)] versus the instantaneous absorbed intensity during a single laser pulse,* I_0 = 5×10^{14} W/cm^2, f = 0.1 *on 404-μm-diameter glass targets; solid target (———), 6-μm-wall shell target (- - -). Arrows mark 100-ps time intervals starting at 200-ps code time, and P denotes the peak of the laser pulse at 773 ps.*

E3440

illustrated in Fig. 23.12 for a solid glass sphere and a 6-μm-thick glass shell target. The mass-ablation rate was calculated by following the progress of the 500-eV isotherm, as referenced to the original Lagrangian frame.

$$\dot{m} = \rho\Delta r/\Delta\tau \qquad (1)$$

where ρ is the material density, and Δr is the thickness of material progressively heated to 500 eV in a time $\Delta\tau$. The 500-eV isotherm was chosen as a characteristic temperature for Si line emission in the 2.0- to 2.5-keV range, which was used as a diagnostic in the experiments described later. The value of $\dot{m}(t)$ derived from the 300-eV or 1-keV isotherm is essentially the same as for the 500-eV isotherm, with peak values occurring marginally earlier and later in time, respectively. This is characteristic of the steep classical heat front in the overdense material.

The noteworthy features of the curves in Fig. 23.12 are that $\dot{m}$ does not have the same scaling with absorbed intensity (I_A) on the rising and falling edges of the laser pulse and that the peak value of $\dot{m}$ is achieved prior to the peak values of both the incident and absorbed intensities. These features are even more pronounced for the glass shell compared to the solid target. A similar dependence of $\dot{m}$ on I_A has been observed in simulations with other flux limiters, as well as for targets of different diameters and different Z.

Our efforts to use the simulations to generate scaling laws of the form $\dot{m} \propto I_A^x R_A^y$ (as in Ref. 1), where R_A is the 500-eV isotherm radius, have been successful only for individual cases and then only for moving-shell targets. On solid glass spheres the excursion of R_A during the laser pulse may range up to 30% of the initial target radius, but it cannot account for the observed decrease in $\dot{m}$. Larger excursions are observed for higher-intensity laser pulses (5×10^{15} W/cm^2) and for smaller (200-μm)-diameter targets.

At λ = 0.351 μm, the predominant absorption mechanism is inverse bremsstrahlung in the subcritical region, and we can define an energy deposition radius R_D as the weighted average absorption radius. Typically, R_D lies between the critical and quarter-critical density radii, but inside the peak temperature (∇T = 0) surface. Defining $\Delta R = R_D - R_A$ as the separation between the energy deposition and ablation surfaces, we find the scaling laws for glass targets

$$\dot{m} \propto I_A^{0.5} \times R_A^{1.4} \times \Delta R^{-0.06} \quad \text{for } f = 0.02$$

$$\dot{m} \propto I_A^{0.65} \times R_A^{1.3} \times \Delta R^{-0.3} \quad \text{for } f = 0.04$$

$$\text{and} \quad \dot{m} \propto I_A \times R_A \times \Delta R^{-0.73} \qquad \text{for } f = 0.40$$

The scaling at f = 0.1 is similar to that at f = 0.4. The magnitude of ΔR is partially dependent on the target size and composition. For moving-shell targets ΔR increases monotonically throughout the laser pulse, but

for solid spheres ΔR is approximately constant after the peak of the laser pulse. We also note that ΔR is proportional to the density scale length L_D at R_D — and perhaps L_D is a more meaningful parameter for the scaling laws, as it affects energy deposition in the corona directly. Another factor that contributes to decreasing $\dot{m}$ is that the fraction of the absorbed energy deposited outside the $\nabla T = 0$ surface increases during the laser pulse.

As suggested in Ref. 1, inverse bremsstrahlung leads to reduced $\dot{m}$ and reduced ablation pressure compared to an energy dump at critical density. More of the laser energy is dissipated at subcritical densities, flowing more directly into blowoff kinetic energy. Also, ΔR is larger because R_D is larger. From Ref. 1 we note that the ablation pressure has a much weaker scaling with radius than $\dot{m}$ does, and our simulations do show that the pressure at the 500-eV isotherm scales with I_A on both the leading and trailing edges of the pulse for the solid targets.

In light of the above simulations, care must be taken when plotting $\dot{m}$ obtained from time-resolved x-ray spectroscopy versus absorbed intensity. Using a pulse-averaged I_A will result in an underestimate in the value of $\dot{m}$ (I_A). To avoid such problems, the time-varying values of $\dot{m}$ should be plotted using the instantaneous value of I_A.

Experiments

The primary diagnostic for our mass-ablation-rate measurements was time-resolved x-ray spectroscopy.[9,10] The experiments were carried out using 6 and 12 UV ($\lambda = 0.351$-μm) beams of the OMEGA laser system at incident irradiances of $I_o = 1 \times 10^{14}$ to 4×10^{14} W/cm^2. The laser pulse had a Gaussian temporal profile with a 600- to 750-ps FWHM. Two types of targets were used in these studies. One set consisted of empty glass microballoons ($\sim$230-μm diameter) with a 1-μm-thick wall. These shells were coated with CH (1- to 8-μm thick) and then overcoated with a 150-Å layer of Au to provide an initial x-ray time marker. The thickness of the Au layer was increased to 300 Å for the 12-beam target shots. The second set of targets were solid glass spheres ($\sim$200-μm diameter) coated with three layers: 1.5-μm CH, 0.05-μm Al, and 1.5-μm CH.

An elliptically curved PET crystal analyzer was used to disperse the x-ray spectrum (1.7- to 2.7-keV range) onto the slit of the x-ray streak camera. Spectral and temporal resolutions were $E/\Delta E$ $\sim$600 and 15 ps, respectively. Perspective plots of the x-ray intensity from streak records for 6- and 12-beam target shots, showing the Au and Si line emission and the implosion time, are presented in Fig. 23.13. The mass-ablation rate through the CH layers of known thickness was measured from the time delay between the start of the Au or Al line emission to the onset of the Si emission from the glass substrate. In all of the target shots where we could measure $\dot{m}$, the CH layer ablated during the rising edge of laser pulse. Thicker CH layers (6–8 μm) did not appear to burn through.

(a)

Time (ns)

1.5

1.0

Implosion

0.5

Si emission

0.0

Au emission

Si 1s-3p (5.22 Å)
Si 1s²-1s3p (5.68 Å)
Si 1s-2p (6.18 Å)
Si 1s²-1s2p (6.65 Å)

(b)

Time (ns)

1.5

1.0

Implosion

0.5

Si emission

0.0

Au emission

Si 1s-3p (5.22 Å)
Si 1s²-1s3p (5.68 Å)
Si 1s-2p (6.18 Å)
Si 1s²-1s2p (6.65 Å)
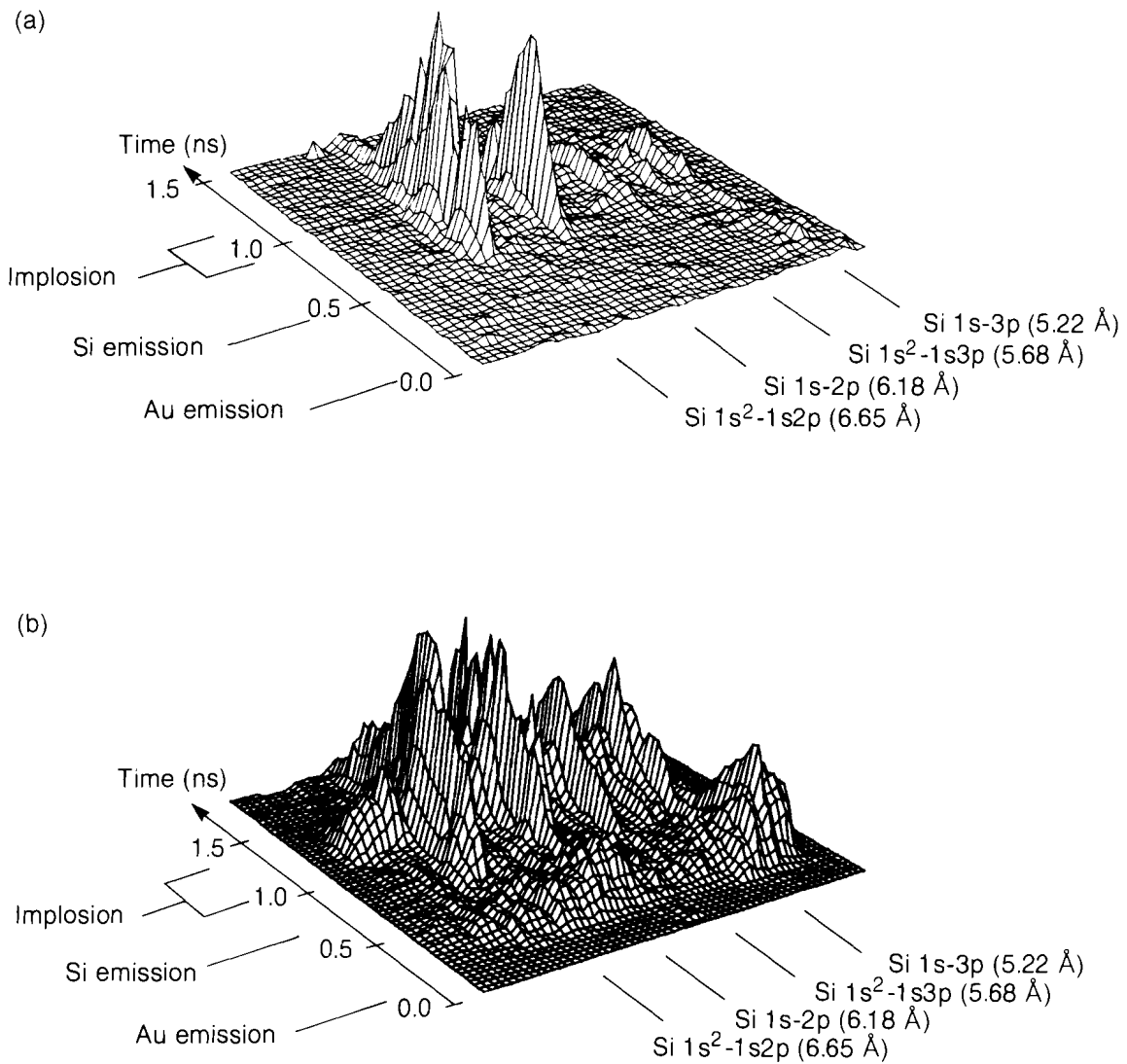
E3441

Fig. 23.13
Perspective plots of the x-ray intensity, as recorded by the streak camera. Correction for the spectrometer response function would increase the intensity on the long-wavelength side by 40%.
(a) 150-Å Au on 4-μm CH on 1.0-μm glass shell target. Diameter is 229 μm at $I_0 = 2.8 \times 10^{14}$ W/cm² with 6-beam irradiation.
(b) 300-Å Au on 3-μm CH on 1.0-μm glass shell target. Diameter is 289 μm at $I_0 = 4.2 \times 10^{14}$ W/cm² with 12-beam irradiation.

In order to construct a meaningful plot of $\dot{m}$ versus I_A, we require knowledge of the absorbed laser intensity during the CH burn-through time of interest. This was inferred from careful comparisons of the streak data with the *LILAC* code simulations, since we could not measure directly the absorption fraction as a function of time nor relate the x-ray emission to the incident laser pulse. We assumed that if the overall predicted absorption of the laser energy agreed with the experimental measurement, then the code could be relied upon to predict the instantaneous absorbed laser intensity during the pulse. Typically, a flux limiter of $f = 0.04$ was required to match the absorbed fractions. We also assumed that the hydrodynamic implosion time predicted by the code for the shell targets was correct. Knowledge of the implosion time allowed us to relate the x-ray emission on the streak record to the incident laser pulse, because the implosion of the glass shell produces a broad and intense spectral feature on the x-ray streak records. This x-ray burst is characteristic of the higher temperatures and densities achieved during the stagnation of the glass shell and lasts ~ 150 ps. The accuracy of the implosion time was checked by calculating the predicted absorbed laser energy up to a time corresponding to the onset of the Au emission, as measured on the streak record. The calculated absorbed laser energy was in the range $3.0 - 5.5$ J (Fig. 23.14), which corresponds to a time window of ~ 80 ps. Conservatively, this implies a 100-ps accuracy on our timing fiducial technique. By including a ± 50-ps jitter in the streak record timing, we obtain a timing fiducial with 150-ps accuracy for the solid-sphere targets.
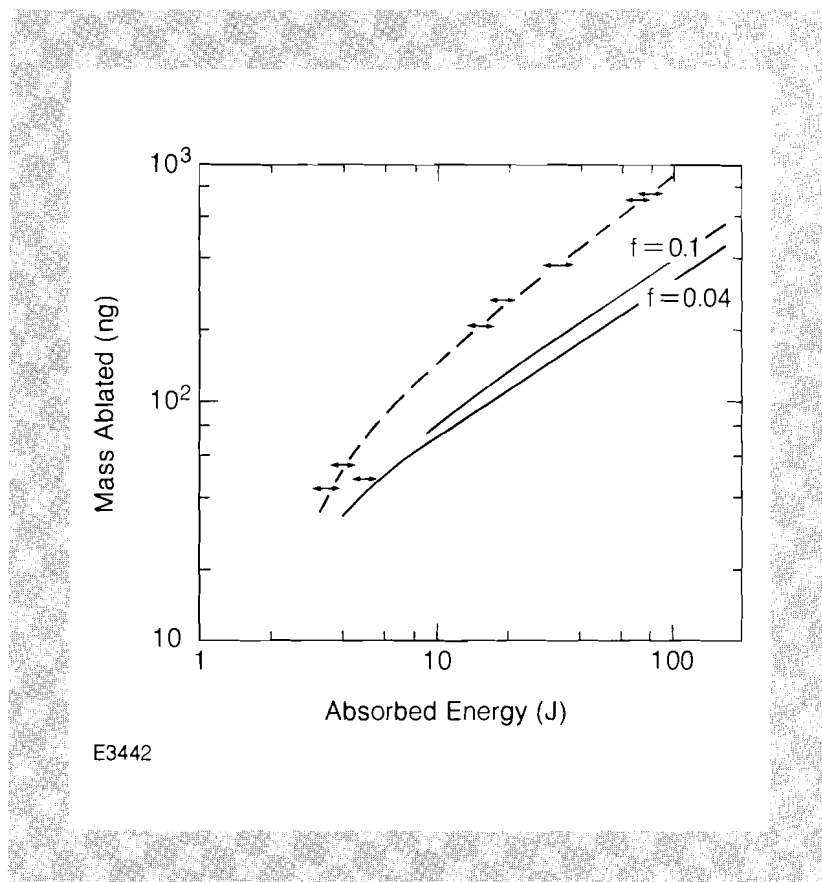
Fig. 23.14
Ablated mass versus absorbed energy for 6-beam irradiation of multilayer targets. The total mass outside the glass substrate is assumed to have been ablated. Solid lines are LILAC *simulations for the mass outside the 500-eV isotherm. Data points at ~ 4 J absorbed energy are for the ablation of the outer Au layer only.*

In Fig. 23.15, we present the scaling of the measured mass-ablation rate versus the average absorbed laser intensity during the CH burn-through interval; I_A is derived from the simulations as outlined above. We also include data for $\dot{m}$ for the outer CH layer on the solid targets where I_A is derived using 3 J of absorbed energy for time zero. The time-resolved 6-beam data is in excellent agreement with the time-integrated measurements at $I_A = 7.5 \times 10^{13}$ W/cm^2, which was measured for a similar target diameter.[6] The scaling of $\dot{m}$ with I_A for 6-beam irradiation and $I_A \leq 10^{14}$ W/cm^2 is in reasonable agreement with code predictions, although the magnitude of $\dot{m}$ is a factor of 2 higher than that predicted for uninhibited transport (f = 0.4). The scaling of $\dot{m}$ with I_A derived from the time-integrated x-ray spectroscopy of Ref. 6 is much weaker than reported here.

E3443
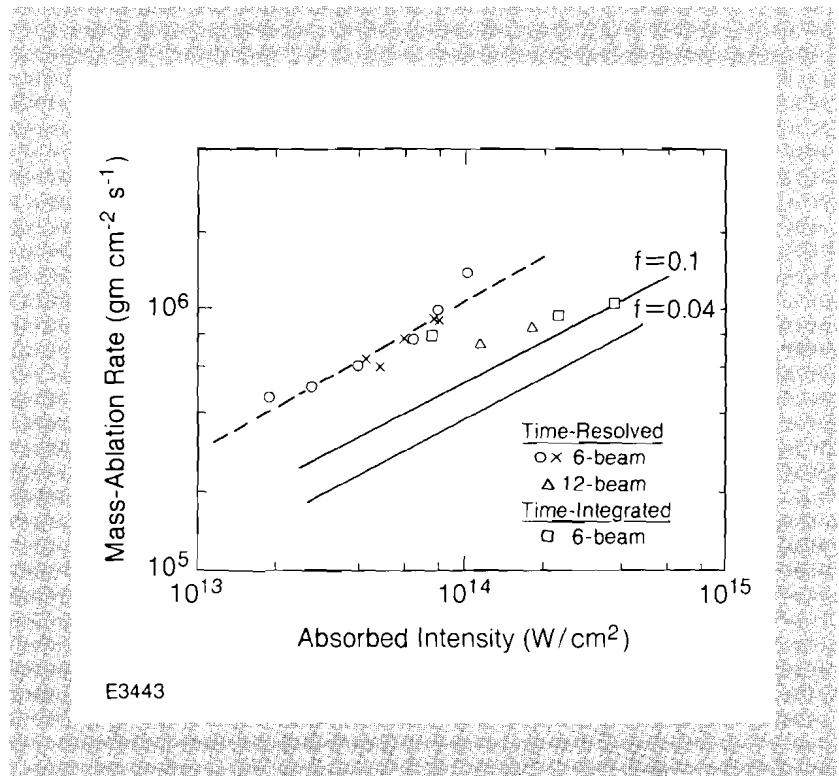
Fig. 23.15
Mass ablation rate versus absorbed intensity at $\lambda = 0.351$ μm. Compared are results from this study (- - -), time-integrated measurements from Ref. 6, and LILAC simulations at f = 0.1 and f = 0.04 for the rising edge of the pulse.

Part of the discrepancy in the measured and calculated values of $\dot{m}$ can be attributed to irradiation nonuniformities. X-ray pinhole pictures of the targets irradiated with 6 beams have shown large-scale x-ray intensity variations across the target surface.[11] Time-resolved imaging of the x-ray emission from the target has also confirmed the existence of discrete hot spots. A detailed computation of the irradiation uniformity on target using measured beam profiles shows that a few percent of the laser energy is absorbed at an intensity greater than three times the average intensity.[12] Given the amount of energy in the hot spots and the sensitivity of our diagnostic—Au emission can be detected with only 2% of the total absorbed energy level from Fig. 23.14—the value of $\dot{m}$ obtained using time-resolved spectroscopy should be characteristic of the absorbed intensity in the hot spots. A shift of our experimental points in Fig. 23.15 by a factor of 3 in I_A results in reasonable agreement with code predictions for f = 0.1. Under the assumption that the laser

energy distribution on target is the same for the approximately constant diameter targets used in these studies, the measured scaling of $\dot{m}$ with I_A should be valid. Similarly, the discrepancy between the measured and calculated values of the amount of mass ablated during the laser pulse in Fig. 23.14 can be attributed to the burn-through of only small areas of the CH coating generated by the hot spots in the irradiation pattern.

With 12 beams, the irradiation uniformity should be improved, and we do observe a significant decrease in the magnitude of $\dot{m}$ (see Fig. 23.15). Further evidence for the decrease in $\dot{m}$ with the more uniform 12-beam irradiation are the burn-through curves presented in Fig. 23.16, as measured by the time-integrating channel of the x-ray spectrometer.[10] Here we plot the absolute energy in the Si^{+12} $1s^2 - 1s2p$ and Si^{+13} $1s$-$3p$ lines as a function of CH overcoat thickness. The 300-Å Au layer on two of the targets was assumed to have an areal mass density equivalent to 0.5 μm of CH, although the effective thickness of the Au layer is greater than this due to radiation cooling in the higher-Z material. The projected burn-through thickness of ≤ 5 μm of CH is much less than the 9 μm of CH interpolated at $I_o = 3 \times 10^{14}$ W/cm^2 from the 6-beam data.[6] This difference cannot be accounted for strictly by the difference in burn-through depth between shells and solids since the onset of the Si emission for our data occurs before the peak of the laser pulse, where the differences in $\dot{m}$ are small.

E3444
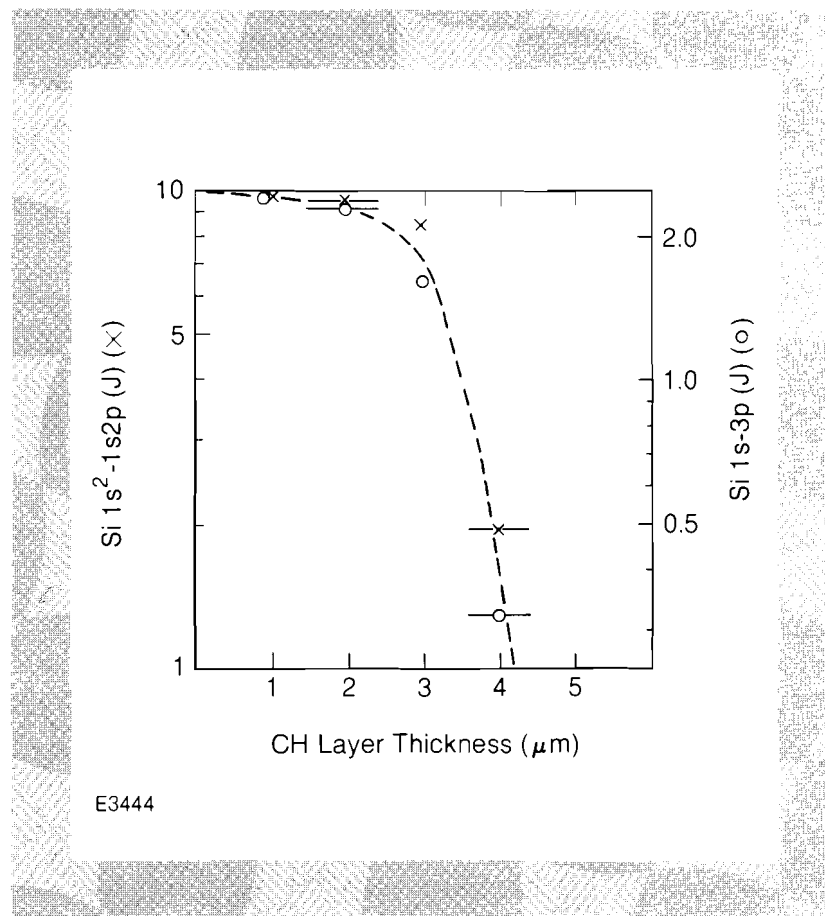
Fig. 23.16
Burn-through curves for CH and Au/CH on glass targets with 12-beam irradiation at $I_o = 4 \times 10^{14}$ W/cm^2 for Si Heα(x) and Si Hβ(o) x-ray resonance lines.

Although we do not have any direct measurements of the mass-ablation rate on the trailing edge of the laser pulse, we do not observe any Si line emission on the streak records for the 6-beam shots on targets with 6- and 8-μm-thick overcoats of CH. This is consistent with the predicted decrease in $\dot{m}$ that starts before the peak of the laser pulse, as illustrated in Fig. 23.12. Using the timing fiducial method outlined above, we estimate that the onset of the Si line emission for a target with a 4-μm CH overcoat occurs ~50 ps before the peak of the laser pulse. If there had been a symmetric scaling of $\dot{m}$ with I_A on the leading and trailing edges of the pulse, we should have observed the Si line emission from the targets with the thicker CH coatings. In addition, if we extrapolate the experimental data in Fig. 23.14 to the mass of these CH layers, the absorbed laser energy on these target shots was sufficient to produce some Si line emission.

Consideration must also be given to the probability of lateral thermal smoothing of the hot spots in the intensity distribution on the target, which appear to dominate the burn-through and $\dot{m}$ measurements with 6-beam irradiation. The amount of smoothing depends on the fractional separation distance $\Delta R/R_o$, where R_o is the target radius.[13] For the imploding targets used in this study, the value of $\Delta R/R_o$ is ~0.2 by the peak of the laser pulse. A value of ~0.3 is predicted by the peak of the laser pulse for the 90-μm-diameter targets irradiated at 10^{15} W/cm^2 in Ref. 6. It is suggested that the lower scaling of $\dot{m}$ with I_A in Ref. 6 is the result of thermal smoothing. This smoothing decreases the magnitude of $\dot{m}$ to a level more characteristic of the average intensity on target.

Conclusions

The measurement of the mass-ablation rate in spherical geometry with short-wavelength lasers is influenced significantly by time-dependent effects during the laser pulse. The transport of thermal energy, and therefore $\dot{m}$, is affected by the increasing separation between the energy deposition and ablation surfaces. Irradiation nonuniformities also have a significant effect on mass-ablation-rate measurements using x-ray spectroscopy, as the burn-through seems to be dominated by hot spots. Our experimental measurements of $\dot{m}$ are in agreement with code predictions for the scaling of $\dot{m}$ with I_A on the rising edge of the laser pulse, as shown in Fig. 23.15; only indirect evidence is presented for lower values of $\dot{m}$ on the trailing edge of the laser pulse.

REFERENCES

1. C. E. Max, C. F. McKee, and W. C. Mead, *Phys. Fluids* **23**, 1620 (1980).

2. T. J. Goldsack *et al.*, *Phys. Fluids* **25**, 1634 (1982).

3. J. A. Tarvin *et al.*, *Phys. Rev. Lett.* **51**, 1355 (1983).

4. B. Yaakobi, J. Delettrez, L. M. Goldman, R. L. McCrory, R. Marjoribanks, M. C. Richardson, D. Shvarts, S. Skupsky, J. M. Soures, C. Verdon, D. M. Villeneuve, T. Boehly, R. Hutchinson, and S. Letzring, *Phys. Fluids* **27**, 516 (1984).

5. A. Hauer *et al., Phys. Rev. Lett.* **53**, 2563 (1984).

6. B. Yaakobi, O. Barnouin, J. Delettrez, L. M. Goldman, R. Marjoribanks, R. L. McCrory, M. C. Richardson, and J. M. Soures, *J. Appl. Phys.* **57**, 4354 (1985).

7. R. C. Malone, R. L. McCrory, and R. L. Morse, *Phys. Rev. Lett.* **34**, 721 (1975).

8. Earlier versions of *LILAC* are described in LLE Reports No. 16 and No. 36 (1976).

9. B. L. Henke, H. T. Yamada, and T. J. Tanaka, *Rev. Sci. Instrum.* **54**, 1311 (1983).

10. B. L. Henke and P. A. Jaanimagi, to be published in *Rev. Sci. Instrum.*

11. M. C. Richardson, S. Skupsky, J. M. Soures, W. Lampeter, S. Tomer, R. Hutchison, M. Dunn, and W. Beich, Conference on Lasers and Electro-optics, Technical Digest, paper FK3 (1984).

12. S. Skupsky (private communication).

13. S. E. Bodner, *J. Fusion Energy* **1**, 221 (1981).

2.B Short-Wavelength, Single-Shell, Direct-Drive Pellet Designs

The response of direct-drive targets to irradiation nonuniformity has been investigated for reactor-size targets with laser-driver energies between 1 MJ and 10 MJ. One-dimensional hydrodynamics calculations were performed to examine the scaling of energy production for targets consistent with specific constraints on aspect ratio (for hydrodynamic stability) and on peak laser irradiation (to minimize plasma instabilities). Two-dimensional hydrodynamic simulations were performed to investigate the effects on target performance produced by irradiation nonuniformities from the multiple overlapping laser beams. These calculations concentrated on the effects of the longer-wavelength nonuniformities (spherical harmonic modes $\ell \leq 8$) characteristic of energy imbalance between beams, beam mispointing, and nonideal beam shapes. Shorter-wavelength nonuniformities are presently under investigation; they can create shell deformations that will be amplified

substantially due to the Rayleigh-Taylor instability.[1-3] Constraints imposed by unstable growth have been applied in determining pellet designs with acceptable aspect ratios (shell radius divided by shell thickness). Generically, the targets considered for this study were single-shell pellets consisting of a low-Z ablator material (CH_2), a cryogenic DT fuel layer and an inner region of DT vapor determined by the initial temperature of the cryogenic fuel (Fig. 23.17). The laser irradiation was a shaped, KrF (250-nm) pulse in the energy range of 1–10 MJ (Fig. 23.18).

TC1623
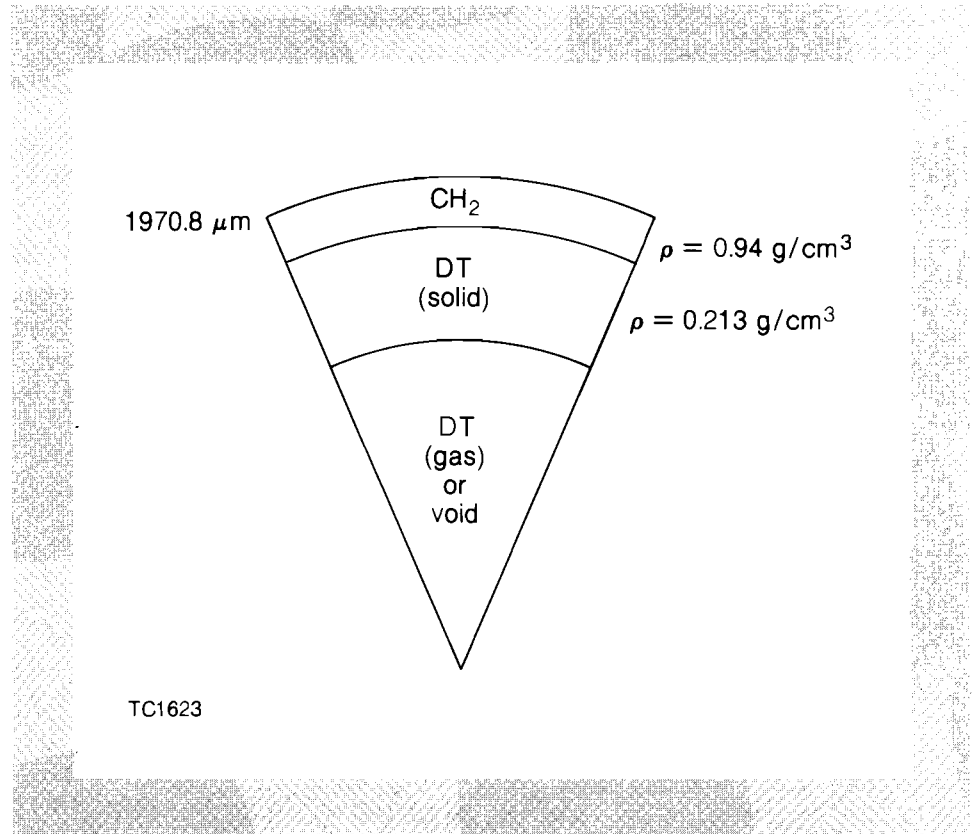
Fig. 23.17
1.6-MJ, single-shell target.

The issue of irradiation nonuniformity from multiple overlapping beams must be addressed for any direct-drive reactor system and pellet design study.[4-8] Typically, it is believed that variations in energy deposition on target should be less than ~1% rms[9,10] to prevent severe degradation of pellet performance due to shell deformation and subsequent core disruption. Simulations have shown that high irradiation uniformity can be obtained for direct-drive systems, using typical reactor focusing optics, by proper attention to the number and placement of individual beams[11] and by focusing each beam such that it initially irradiates approximately a complete hemisphere. (With the use of such highly non-normal laser irradiation a ray-trace algorithm[12] must be used to treat both the refraction of the incident laser light and deposition of laser energy in the plasma atmosphere. Changes in the critical-surface position and plasma-atmosphere size during the implosion result in changes in the illumination uniformity pattern, both in magnitude and shape, throughout the laser pulse.)
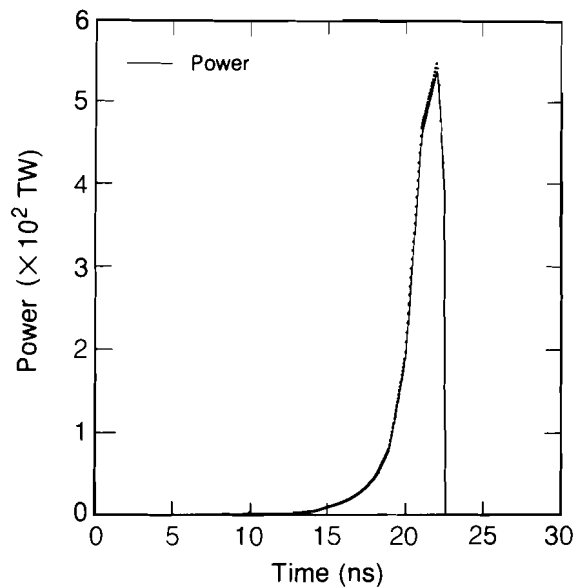
Fig. 23.18
Time-tailored laser pulse used for the
1.6-MJ design.

One-Dimensional Results

The 1-D pellet designs were carried out using the University of Rochester's hydrocode *LILAC*. *LILAC* contains Lagrangian hydro-dynamics, tabular equation-of-state (SESAME[13]) thermonuclear burn, multigroup fusion product transport, and multifrequency-group radiation transport. The opacities used in the radiation transport calculation were obtained from reducing 2000 frequency group LTE LANL Astrophysical Library[14] tables to a desired group structure (~50 groups are used in most *LILAC* simulations). Laser deposition is done using a geometrical optics ray-trace[12] algorithm with energy deposition by inverse bremsstrahlung along each ray path. Flux limitation of electron thermal transport[15] is incorporated as a harmonic mean with the Spitzer-Härm electron thermal conductivity. [For all of the simulations presented in this report, the value of the flux limiter (f) was set to 0.04, with the maximum permitted heat flux given by $q_{max} = f n_e kT(kT/m_e)^{1/2}$.]

Some of the constraints imposed upon the designs are discussed below.

1. In-Flight Aspect Ratio

The in-flight aspect ratio is considered to be a measure of a target's ability to withstand shell breakup due to the Rayleigh-Taylor instability.[1-3,16] The definition[17] of the in-flight aspect ratio A(t) is given by $A(t) = \bar{R}(t)/\Delta R(t)$ where $\bar{R}(t)$ and $\Delta R(t)$ are a characteristic shell radius and thickness at time t. The value of $\Delta R(t)$ is found by first determining the radial location and value of the peak material density in the pellet. Next the radial locations are found both ahead and behind the peak

where the density is one e-folding below the maximum. The distance between the two locations defines $\Delta R(t)$, and $\bar{R}(t)$ is the average of the locations. One-dimensional simulations have shown that this definition accounts for ~75% of the imploding shell mass. This region represents the material that acts as the cold fuel layer and pusher surrounding the "spark-plug" region of the target. The effect of the Rayleigh-Taylor instability on the material identified by the above method is critical to target performance. The in-flight aspect ratio serves only as a guideline by which 1-D pellet designs can be judged as conservative or optimistic, until multidimensional calculations are available.

2. Convergence Ratio

Two convergence ratios have been considered in designing the single-shell pellets. The first is simply the initial radius of the DT fuel-pusher interface divided by the minimum radius obtained for that interface during the implosion. (If this interface is ablated during the implosion, we take the minimum radius to be that of the outermost unablated DT zone.) This definition serves as a measure of the approximate distance the ablator travels during the implosion and is used to estimate the number of possible e-foldings an infinitesimal perturbation would experience.

A second convergence ratio is defined to characterize the spark-plug region, which ignites the bulk of the thermonuclear fuel mass. Hydrodynamic simulations show that the spark plug for these pellets is primarily composed of the material from the initial low-density vapor region of the pellet. Thus, the spark-plug convergence ratio is defined as the initial radius of the interface between the gas and the cryogenic layer divided by the radial location of this interface at the time of ignition. The spark-plug convergence ratio is used in conjunction with the size of the spark-plug region at the time of ignition to estimate the possible effects of instability during the deceleration phase of the implosion.

3. Laser Irradiance

To prevent the generation of energetic electrons from plasma processes,[18,19] the peak laser irradiance was kept below a few times 10^{15} W/cm^2 at the critical surface. The peak irradiance levels were reached only near the end of the laser pulse. Since reactor-size plasma scale lengths have not yet been investigated in the laboratory, the possible effects of plasma phenomena at high laser intensities are not well understood.

4. Illumination Uniformity

Calculations[11] for direct-drive illumination uniformity have examined different laser configurations containing up to 96 beams. Typically, for all configurations considered, optimal uniformity is obtained at a focal distance ~ 0.9 times the distance for tangential focus (as measured from the target center). Tangential focus is defined as the focal position where a beam subtends an entire target hemisphere; it is at a distance of $2 \times f^\# \times R$, where $f^\#$ is the f-number of the final optical element and R is the target radius. As the target radius (or more correctly, the critical-density radius) decreases during the implosion, the amount of the target subtending each beam will change, resulting in a change in uniformity.

The strategy used here was to focus initially at the point of optimum uniformity. As focusing conditions deviate from optimum during the implosion, the irradiation nonuniformity will increase, but so will the size of the plasma atmosphere surrounding the target, permitting smoothing of some nonuniformities in energy deposition by thermal conduction. (For a system with more than ~ 60 beams, the increase in nonuniformity during the implosion was found to be relatively small). For all the 1-D designs considered here, f/20 optics was used in the ray-trace algorithm with the initial focal position at 36 times the target radius.

5. Target Fabrication

It must be noted that all of the pellet designs considered here are not consistent with current target fabrication technology. The large DT, gas-fill pressure that would exist at room temperature inside the ablator shell exceeds present fabrication limits. (Present technology is limited to approximately 100 atm, while targets considered here contain nearly 600 atm of DT at room temperature.)

A summary of the target design characteristics for targets at 1.6 MJ and 4.1 MJ is shown in Table 23.I. Both cases use the generic target and pulse shape of Figs. 23.17 and 23.18. (The 4.1-MJ design is a scaled-up version of the 1.6-MJ design—i.e., larger target and longer pulse.) The variation in pellet gains with incident laser energy for the single-shell, 1-D designs considered in this study is shown in Fig. 23.19. [The shaded band about the central line indicates the changes that were observed by varying the value of the flux limiter (f) between 0.03 and 0.06.] No attempt was made to adjust target parameters to optimize the gain when the flux limiter was changed. From Fig. 23.19 it can be

Table 23.I
Target design characteristics and results.

Target Design Characteristics and Results

	1.6 MJ	4.1 MJ
Energy Supplied	1.57 MJ	4.09 MJ
Energy Absorbed	1.26 MJ	3.51 MJ
Absorption Fraction	0.80	0.86
Peak Laser Intensity	1.1×10^{15} W/cm^2	1.8×10^{15} W/cm^2
Peak Laser Power	600 TW	800 TW
Hydrodynamic Efficiency	10%	10%
Peak Fuel Mass-Averaged Implosion Velocity	35.0 cm/μs	30.0 cm/μs
Peak Fuel $<\rho R>$	2.56 g/cm^2	4.0 g/cm^2
Convergence Ratio	13.8	10.7
Convergence Ratio (spark plug)	70.0	80.0
In-Flight Aspect Ratio	80.0	65.0
Gain (Total TN Products)	68.0	120.0
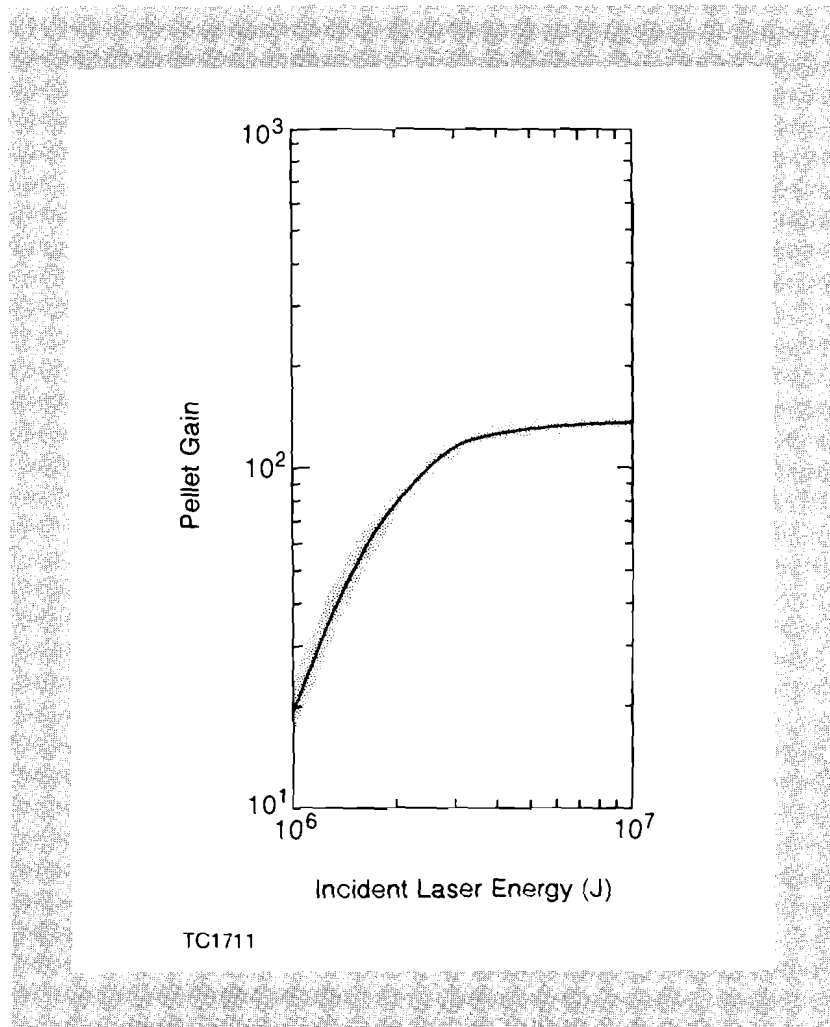
Fig. 23.19
Energy gain versus incident KrF laser energy for single-shell, direct-drive pellet designs.

seen that the pellet gain levels off to ~120 for incident energies above ~4.0 MJ.

In order to estimate the effect of mixing between the plastic pusher and the igniting DT during shell deceleration and burn, we have applied a free-fall argument. By extrapolating the trajectory of the plastic fuel interface to 80% of the minimum fuel core radius, a time is estimated that corresponds to the time at which half the fuel mass would be mixed with ablator material. Thermonuclear (TN) yield that would accrue after this time is ignored in the calculation. The result of this estimate is that 98% of the TN yield is released before the plastic mixes with half the fuel mass. This may, however, still overestimate the yield. Pellets of this generic type (i.e., a large thickness of cryogenic DT and a thin ablator layer) effectively use the outer region of the fuel as the pusher during final core assembly. Most, if not all, of the plastic has been ablated once the burn has begun. Therefore, the more important questions with respect to mixing and possible TN yield reduction for these pellets are (1) the unknown effects of cold DT mixing with hot DT during the spark-plug formation, and (2) bulk mixing of DT and its effect on pellet performance once the burn wave has begun to propagate outward from the spark region.

Two-Dimensional Results

The above results have assumed uniform laser irradiation. For multiple beam overlap, there will be some nonuniformities in irradiation. If large enough, they can lead to a distorted compressed core and a reduced target gain. The effects of long-wavelength nonuniformities (ℓ = 2,4,8) have been calculated for the 1.6-MJ design. Modes ℓ = 2 and ℓ = 4 are generally produced by beam energy imbalance and beam mis-pointing. The ℓ = 8 mode is characteristic of the nonuniformity produced in beam overlap by 24–32 beams (even assuming perfectly smooth laser profiles).[4] Nonuniformities in temperature produced by these long-wavelength modes are not expected to be significantly attenuated by thermal smoothing within the target atmosphere and, therefore, will distort the target drive during the entire time of irradiation. Shorter-wavelength nonuniformities can be smoothed by thermal conduction once an adequate plasma atmosphere has been established. However, the distortion produced prior to that time will continue to grow exponentially during acceleration and deceleration of the target shell due to the Rayleigh-Taylor instability.

The effects of nonuniformities were examined using the University of Rochester's 2-D (R-Z) Lagrangian hydrodynamics code *ORCHID*. The laser nonuniformity was applied as a single Legendre mode (ℓ) with varying amplitudes: peak-to-valley amplitudes of 2% and 4% for the ℓ = 2 and 4 cases, and amplitudes of 1% and 2% peak to valley for the ℓ = 8 case.

Characteristic results are presented here for an ℓ = 4 nonuniformity, imposed with peak irradiation on the pole (Z-axis). The time history of the spark-plug formation, ignition, and subsequent burn for the 2% peak-to-valley (σ_{rms} = 0.65%) case is shown in Figs. 23.20 through 23.22. Figure 23.20 displays density contours in g/cm^3; Fig. 23.21 shows ion temperature contours in eV; and Fig. 23.22 displays the velocity vectors showing the fluid motion at four different times. The spark-plug region is forming in the two upper frames of all three figures. In the upper right-hand frame of Fig. 23.22, the material that was initially in the cryogenic DT layer has ignited as indicated by the region of rapidly diverging velocity vectors.

Ignition and thermonuclear burn in these targets proceeds in the following manner. As the implosion reaches the core-assembly phase, the ion temperature in the gas begins to rise due to both PdV work and shock heating. The particles emitted from the gas region initially begin to deposit energy throughout the main fuel layer due to the low $<\rho R>$ at this time. As the main fuel body continues to implode, a point is reached where the $<\rho R>$ rises to values large enough to stop most of the α particles within a short distance into this region. This is the point we refer to as ignition for the pellet designs identified in this study. The ion temperature and $<\rho R>$ in the gas region at this time are of the order of 10 keV and ~0.1 g/cm^2 respectively. In the region where most of the α particles are stopped, the ion temperature is ~2.75 keV while the $<\rho R>$ is ~0.55 g/cm^2 as measured from the target center.

Time = 24.49 ns

Time = 24.50 ns

Time = 24.53 ns

Time = 24.55 ns
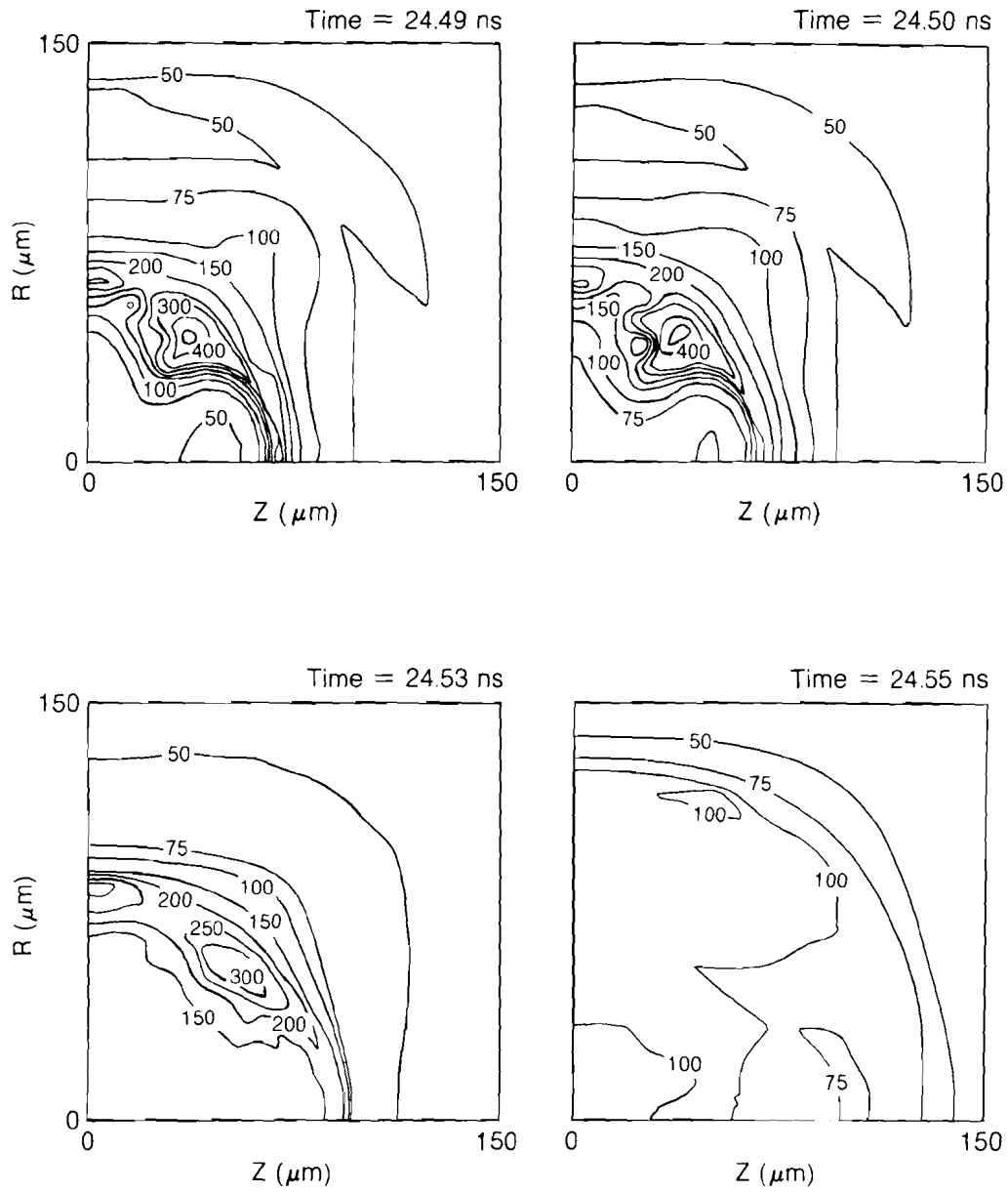
TC1701

Fig. 23.20
Density contours (g/cm³) at various times for the ℓ = 4, 2% peak-to-valley, 1.6-MJ implosion.
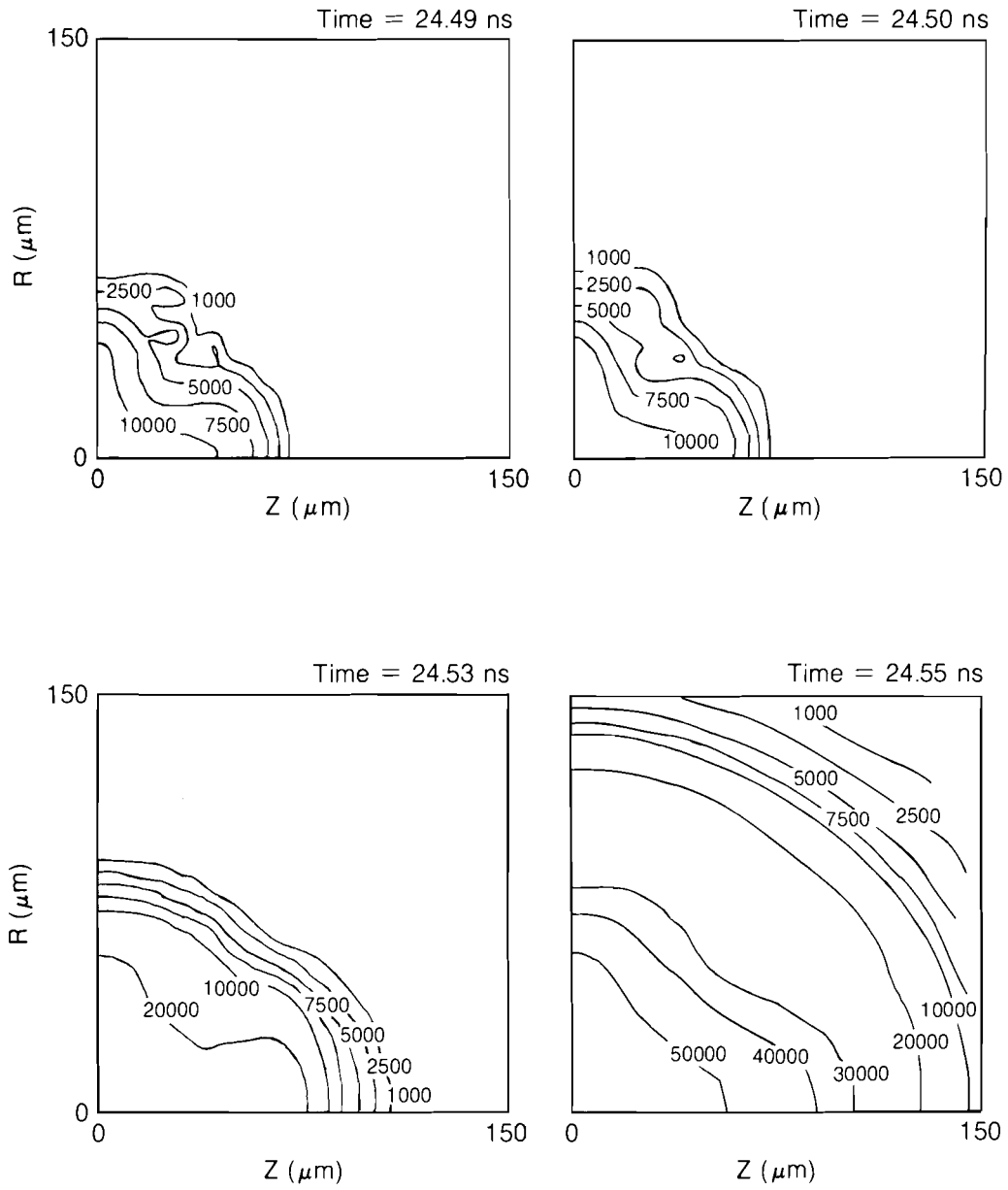
Fig. 23.21
Ion temperature contours (eV) at various times for the $\ell = 4$, 2% peak-to-valley, 1.6-MJ implosion.

TC1703

Time = 24.49 ns   Time = 24.50 ns

Time = 24.53 ns   Time = 24.55 ns
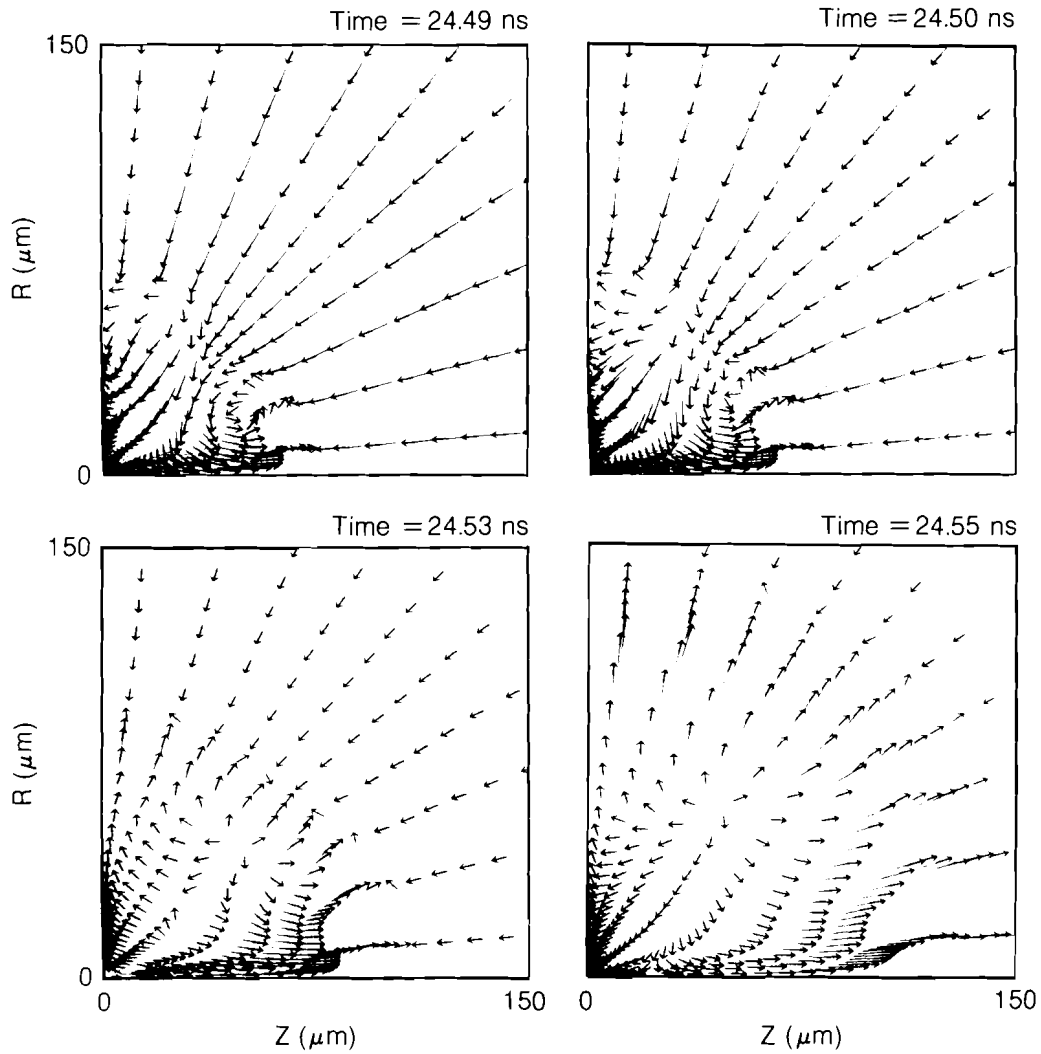
TC1705

Fig. 23.22
Velocity vectors at various times for the $\ell = 4$, 2% peak-to-valley, 1.6-MJ implosion.

At the time of core assembly and burn, the $<\rho R>$ of the core was found to be reversed in phase from the applied illumination perturbation. Figure 23.23 displays $<\rho R>$ versus polar angle (Z axis equals $0.0°$). The left-hand frame of Fig. 23.23 shows the $<\rho R>$ before final core assembly. Note that the $<\rho R>$ phase is that of the applied illumination. The middle frame shows that the phase of the $<\rho R>$ is beginning to change as the spark plug is forming, and the right-hand frame is at the time near peak $<\rho R>$ where the reversal in the applied perturbation amplitude is clearly evident. This reversal begins before the shell

Time = 20.24 ns

Time = 22.00 ns

Time = 24.51 ns

Polar Angle θ (degrees)

Polar Angle θ (degrees)

Polar Angle θ (degrees)

TC1707
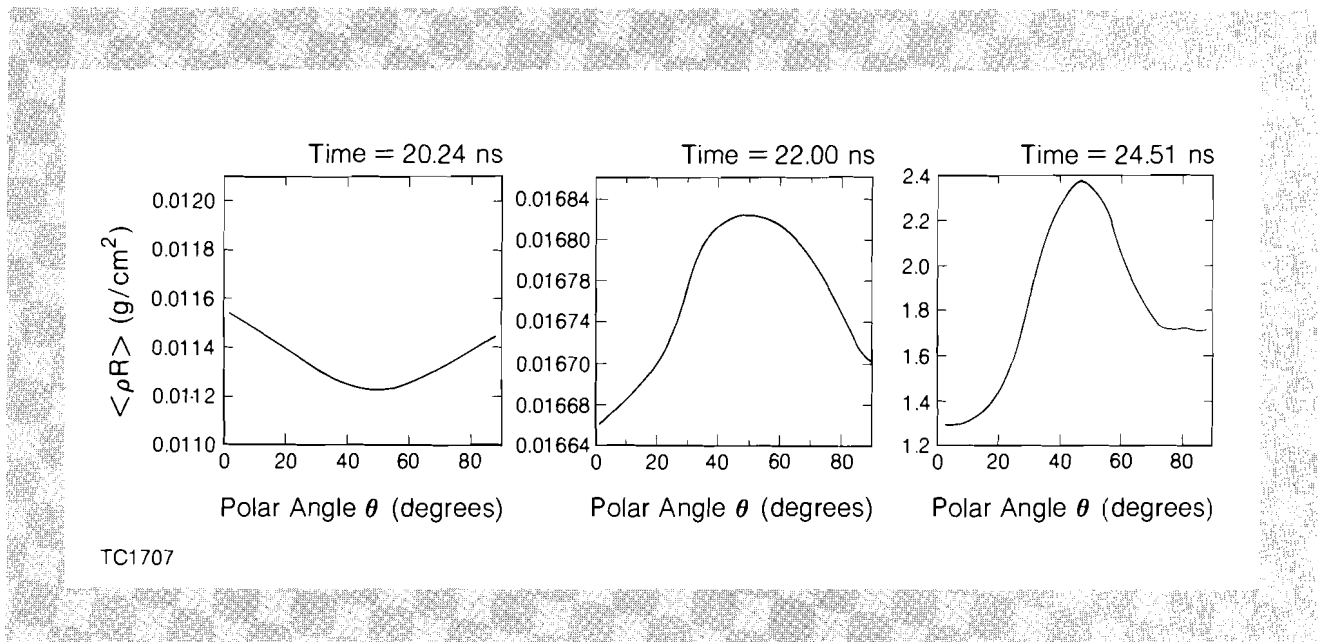
Fig. 23.23
Fuel $<\rho R>$ (g/cm^2) versus polar angle at various times for the ℓ = 4, 2% peak-to-valley, 1.6-MJ implosion.

decelerates and is due to an azimuthal pressure generated by the convergence of the distorted shell. During deceleration, a combination of jetting due to the azimuthal pressure generation and Rayleigh-Taylor unstable growth is responsible for the development of the perturbation near the interface between the gas and cryogenic DT layers seen in Fig. 23.20. The temperature profiles during the core assembly phase also follow the density perturbation early in time (upper two frames, Fig. 23.21). However, once the pellet ignites, the combination of α-particle energy deposition and thermal transport acts to smooth variations in the temperature profiles in the pellet core resulting in a relatively radially propagating burn front.

A summary of the growth of the deformation is shown in Fig. 23.24. Plotted is the maximum-minus-minimum radial location ($\Delta R_{max-min}$) of the Lagrangian interface between the gas region and the cryogenic DT layer versus the average radius ($\bar{R}$) of that interface, for the ℓ = 4, 4% peak-to-valley case. When the average interface location reaches 150 μm, the phase of the perturbation begins to change, resulting in a reduction of $\Delta R_{max-min}$. However, below ~75 μm, the perturbation amplitude of this surface grows rapidly, until ($\Delta R_{max-min}/\bar{R}$) is of the order of unity (see Fig. 23.25).

The 2%, ℓ = 4 nonuniformity caused an 8% reduction in target gain. When the illumination perturbation amplitude was increased to 4% peak to valley (σ_{rms} = 1.25%), the pellet failed to ignite. The increased perturbation caused a large quantity of colder DT to be forced into the spark-plug region, thereby (1) cooling the spark plug by conduction and (2) converting its internal energy into kinetic energy as it moved out of the way of the incoming colder fuel. This can be seen in Fig. 23.25, which shows a comparison of the ℓ = 4, 2% and 4% peak-to-valley cases at the time of ignition. (The shaded regions on the grid plots represent the initial low-density fill-gas material.) The larger disruption of the spark-plug region is clearly evident for the 4% peak-to-valley case.
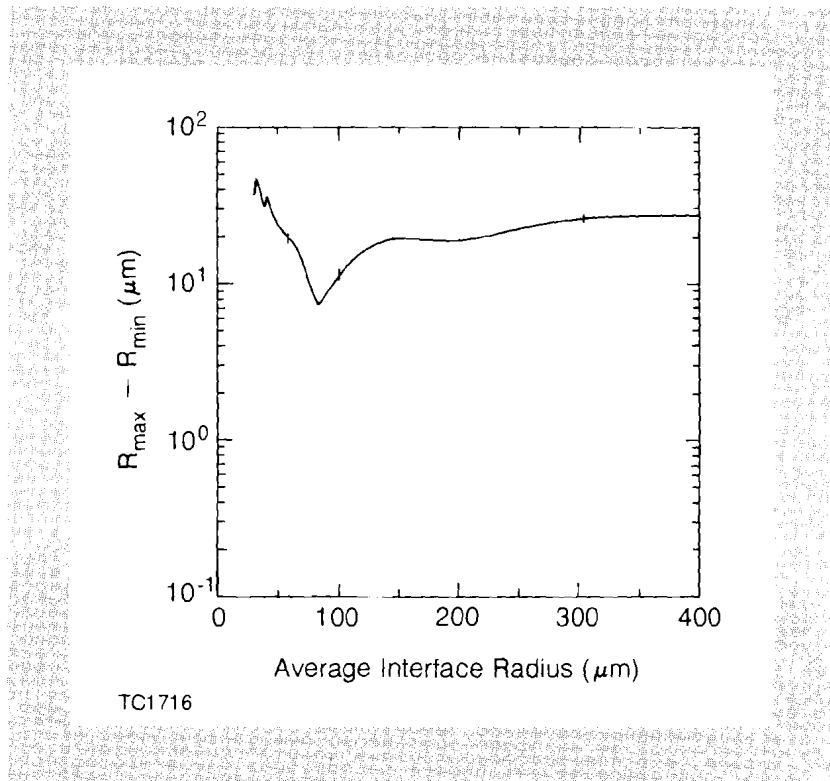
Fig. 23.24
Maximum-minus-minimum radius of the gas-solid interface versus radius for the $\ell = 4$, 4% peak-to-valley case.

A summary of the degradation in target gain with increased irradiation nonuniformity is shown in Fig. 23.26 for the three modes considered. This amount of degradation is not a general result for direct-drive targets, but represents the performance of only a single design. In particular, analysis of the failure of the 4%, $\ell = 4$ case suggests that a substantial target gain would have occurred for a small increase in laser energy. The general trend is that the shorter modes are the most dangerous, and that any thermal smoothing of the nonuniformity that might have occurred is compensated for by Rayleigh-Taylor growth in the target.

Future Work

One possible method of reducing the sensitivity of these types of pellets to irradiation nonuniformities would be to decrease the spark-plug convergence ratio. As an example, Fig. 23.27 displays the spark-plug convergence ratio and pellet-gain versus the DT gas density (which is determined by the DT-layer initial temperature) for the 1.6-MJ design. Note that the spark-plug convergence ratio can be halved without reducing the pellet gain for this design. The response to irradiation nonuniformities of targets with the lower spark-plug convergence ratio is presently under investigation.

A second area requiring further examination is the effect of the Rayleigh-Taylor instability on imploding shells. Due to resolution limitations, such simulations will have to be performed using "conical" sections, with a slip surface between $\theta = 0°$ and $90°$. These runs cannot be taken to final core implosion due to incorrect boundary conditions about the slip surface. However, these simulations will

Grid Plots
2% Peak-to-Valley

Density Contours (g/cm^3)
2% Peak-to-Valley

4% Peak-to-Valley
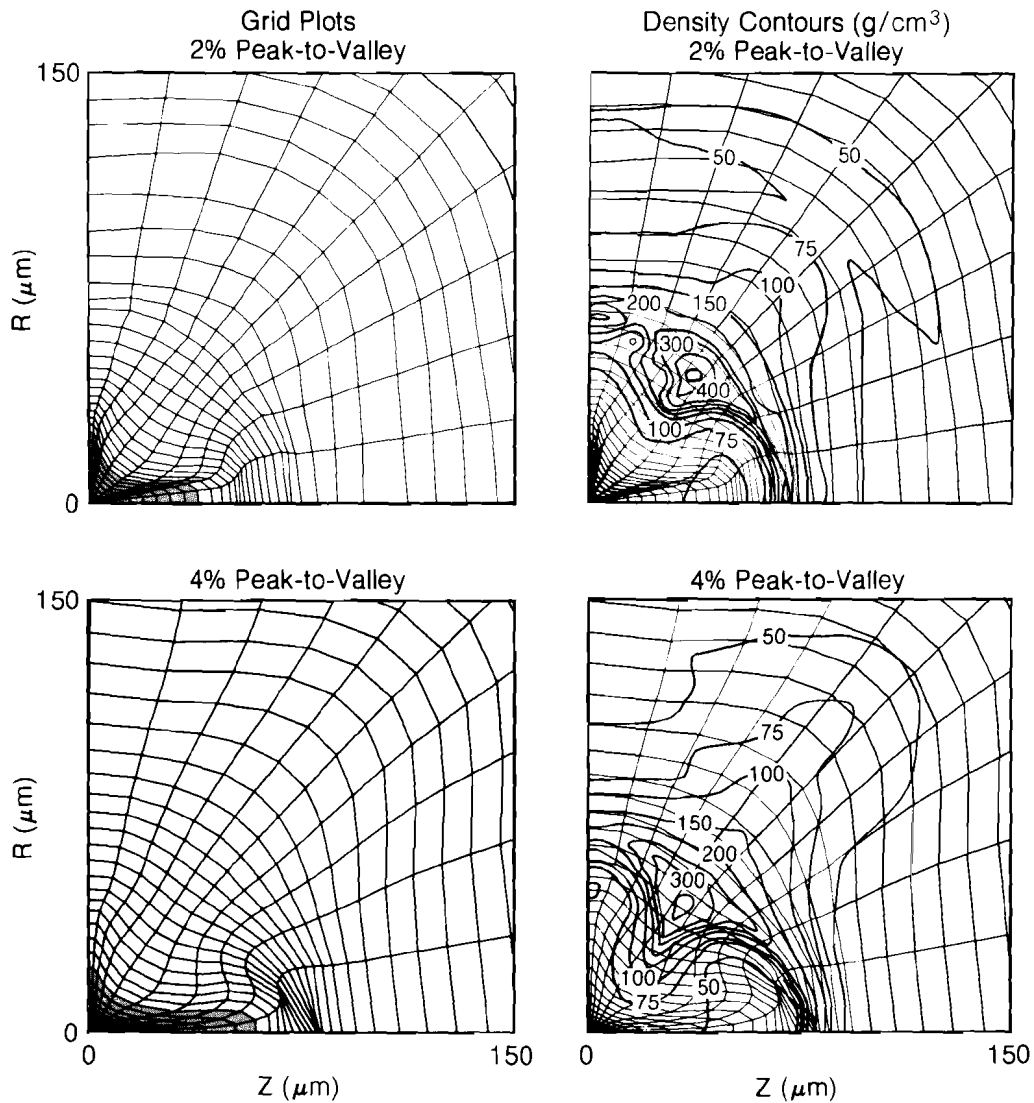
4% Peak-to-Valley

TC1712

Fig. 23.25
Spark-plug region at the time of "ignition" for two $\ell = 4$ cases: one with a 2% peak-to-valley imposed irradiation nonuniformity and the other with a 4% nonuniformity.

address the effects of short-wavelength Rayleigh-Taylor unstable growth on the shell (pusher) during the rapid acceleration phase of the implosion, before the effects of spherical convergence become important. These studies will also help to determine more accurate hydrodynamic limitations, which will be used in the examination of 1-D pellet designs.
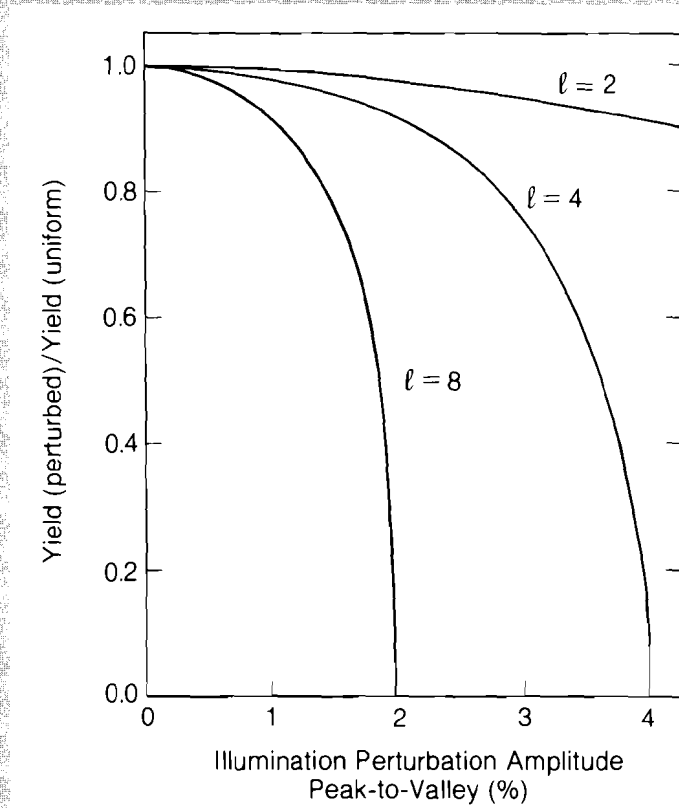
TC1794

Fig. 23.26
Yield reduction versus illumination pertur-
bation for the 1.6-MJ pellet designs.
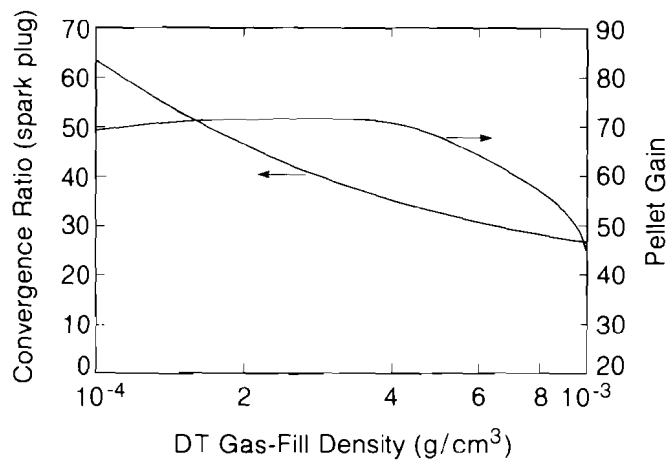
TC1717

Fig. 23.27
Pellet convergence ratio and pellet gain at
the time of ignition versus DT gas-fill den-
sity for 1.6-MJ pellet designs.

Work is also under way to examine methods of reducing the in-flight aspect ratios of the 1-D designs identified in this study. A reduction in the in-flight aspect ratio will be beneficial when considering the effects of short-wavelength, Rayleigh-Taylor unstable growth. However, even with reductions in the in-flight aspect ratio, the effects of long-wavelength perturbations of the order of $\ell \leq 12$ will still be important. Their "feed-through" to the inner surface of the shell will not be greatly reduced by decreases in the in-flight aspect ratio; their effect on the final core assembly and pellet performance may remain essentially unchanged even if the in-flight aspect ratio is reduced by factors of 2.

ACKNOWLEDGMENT

REFERENCES

1. G. S. Fraley, W. P. Gula, D. B. Henderson, R. L. McCrory, R. C. Malone, R. J. Mason, and R. L. Morse, in *Plasma Physics and Controlled Nuclear Fusion Research, Tokyo, Japan* (International Atomic Energy Agency, Vienna, 1974), Vol. 2, p. 543.

2. C. P. Verdon, R. L. McCrory, R. L. Morse, G. R. Baker, D. I. Meiron, and S. A. Orszag, *Phys. Fluids* **25**, 1653 (1982).

3. W. C. Mead and J. D. Lindl, LLNL Report UCRL-78457 (1976).

4. S. Skupsky and K. Lee, *J. Appl. Phys.* **54**, 3662 (1983).

5. Lawrence Livermore Laboratory Laser Program Annual Report UCRL-50021-74, p. 219 (1975).

6. J. E. Howard, *Appl. Opt.* **16**, 2764 (1977).

7. A. J. Scannapieco and H. Brysk, *J. Appl. Phys.* **50**, 5142 (1979).

8. K. Lee, R. L. McCrory, and R. Hopkins, Laboratory for Laser Energetics Report No. 88 (1981).

9. S. E. Bodner, *J. Fusion Energy* **1**, 221 (1981).

10. S. Skupsky, R. L. McCrory, R. S. Craxton, J. Delettrez, R. Epstein, K. Lee, and C. Verdon, in *Laser Interaction and Related Plasma Phenomena*, edited by H. Hora and G. H. Miley (Plenum, New York, 1984), Vol. 6, p. 751.

11. LLE Review **19**, 120 (1984).

12. M. Born and E. Wolf, *Principles of Optics* (Pergamon, New York, 1975), p. 123.

13. B. I. Bennett, J. D. Johnson, G. I. Kerley, and G. T. Rood, Los Alamos National Laboratory Report LA-7130 (1978).

14. W. F. Huebner, A. L. Merts, N. H. Magee, and M. F. Argo, Los Alamos National Laboratory Report LA-6760-M (1977).

15. R. C. Malone, R. L. McCrory, and R. L. Morse, *Phys. Rev. Lett.* **34**, 721 (1975).

16. G. Taylor, *Proc. R. Soc. London, Ser. A* **201**, 192 (1950).

17. J. D. Lindl (private communication).

18. K. Estabrook and W. L. Kruer, *Phys. Rev. Lett.* **40**, 42 (1978); D. W. Forslund, J. M. Kindel, and K. Lee, *ibid.* **39**, 284 (1977).

19. W. L. Kruer, *Comments Plasma Phys. Controlled Fusion* **6**, 167 (1981).

20. P. C. Souers, LLNL Report UCRL-52628 (1979).

21. M. H. Emery, *Bull. Am. Phys. Soc.* **29**, 1231 (1984).

22. S. Skupsky, R. L. McCrory, and C. P. Verdon, *Bull. Am. Phys. Soc.* **26**, 1289 (1984).

23. Lawrence Livermore Laboratory Laser Program Annual Report UCRL-50021-79, Chap. 3 (1979).

2.C Stimulated Raman Scattering in a Collisional Homogeneous Plasma

In the last two decades, the coherent nonlinear interaction of three coupled waves has received considerable attention. It occurs in the process of stimulated Raman scattering (SRS) in the plasma corona that surrounds the fuel pellet in laser-fusion experiments. In this process an incident light wave decays into a Langmuir wave and a scattered light wave. It is important to calculate the amplitudes of the daughter waves for two reasons. First, light energy that is scattered away from the pellet can no longer assist in the ablation process. Second, the breaking of the Langmuir wave generates hot electrons, which can preheat the fuel and thereby reduce the amount of compression.

The standard approach to this problem is to derive evolution equations for the amplitude of each wave, which can then be solved in a variety of ways. For instance, in cases in which the wave amplitudes depend on both space and time, one could use the Inverse Scattering Transform.[1] In temporal problems, the solutions are assumed to be homogeneous in space, and the problem reduces to that of three coupled simple harmonic oscillators whose natural frequency ω_j depends parametrically on the wavenumber k_j. Spatial problems typically involve a constant-amplitude pump wave impinging on a medium which may be finite or semi-infinite in length. One then solves a two-point boundary value problem to determine the steady-state amplitude of each wave.

Here, we consider the temporal problem for SRS in a collisional homogeneous plasma. The electromagnetic waves are collisionally damped while the plasma wave is affected by collisions and a phenomenological

term representing Landau damping. This problem, with a different damping coefficient for each wave, has previously been thought intractable by analytic means.[2] In this article, we formulate a slightly different problem by introducing a driving term into the pump equation. This balances the energy lost by dissipation and permits a steady, spatially uniform oscillation of the pump wave. However, this equilibrium is unstable since the amplitude of the pump wave is above its SRS threshold value. Energy is therefore exchanged between the waves until a new and stable equilibrium condition is reached. Previously,[3] we calculated the steady-state amplitude of each wave when the system was only marginally unstable. Here, the calculation is extended to include the highly unstable regime.

The governing equations for SRS assume their simplest form when written in terms of the action amplitude of each wave. The square of the action amplitude, namely the action density, is defined to be the energy density of each wave divided by its natural frequency, which is proportional to the number density of quanta present in each wave field. The resulting simplification of the basic equations reflects the fact that physically, SRS is the decay (and recombination) of an incident pump photon into a scattered photon and a plasmon. The governing equations are

$$\left(\frac{\partial}{\partial t} + \nu_1\right) A_1 = -icA_2A_3\exp(i\delta t) + \nu_1 A_1(0), \tag{1a}$$

$$\left(\frac{\partial}{\partial t} + \nu_2\right) A_2 = -icA_1A_3^*\exp(-i\delta t), \tag{1b}$$

$$\left(\frac{\partial}{\partial t} + \nu_3\right) A_3 = -icA_1A_2^*\exp(-i\delta t), \tag{1c}$$

where

$$\delta = \omega_1 - (\omega_2 + \omega_3)$$

is the frequency mismatch, and the subscripts 1, 2, and 3 refer to the incident pump wave, the scattered electromagnetic wave, and the plasma wave, respectively. We see that the exchange of energy, made possible by the terms that are quadratic in the wave amplitudes, is modified by the effects of damping and frequency mismatch. Explicit expressions for the coupling constant c, and the damping rates ν_j, can be found in Ref. 1. The initial amplitude of the pump wave is equal to $A_1(0)$, while the daughter waves initially have noise-level amplitudes.

A standard linear analysis of Eqs. (1a)–(1c) shows that the threshold amplitude of the pump, denoted by A_{10}, is given by

$$|A_{10}|^2 = \frac{\nu_2\nu_3}{c^2} (1 + r^2), \tag{2}$$

where $r \equiv \delta/(\nu_2 + \nu_3)$ is the mismatch ratio. When the pump amplitude exceeds its threshold value, the daughter waves grow exponentially in time. The linear growth rate γ is equal to the root of

$$\gamma^2 + [(\nu_2 + \nu_3) - ir(\nu_2 - \nu_3)]\gamma + \nu_2\nu_3(1 + r^2) - c^2|A_1(0)|^2, \tag{3}$$

which has the largest real part. Eventually, nonlinear effects become important and modify the temporal evolution of the system.

Let us now examine the nonlinear interaction. In the absence of damping, Eqs. (1a)–(1c) yield periodic solutions which can be expressed in closed form, in terms of elliptic functions.[4] There is therefore a periodic exchange of energy between the pump wave and its daughter waves, as shown in Fig. 23.28. In this and subsequent figures, we have measured time in units of Ω^{-1}, where Ω is a naturally occurring frequency parameter of the order of ω_p. An explicit expression for Ω is given in Ref. 1. The peak energy of the backscattered wave, which we denote by E_{2p}, is related to the initial energy contained in the pump wave by the familiar Manley-Rowe relationship $E_{2p}/\omega_2 = E_1(0)/\omega_1$.
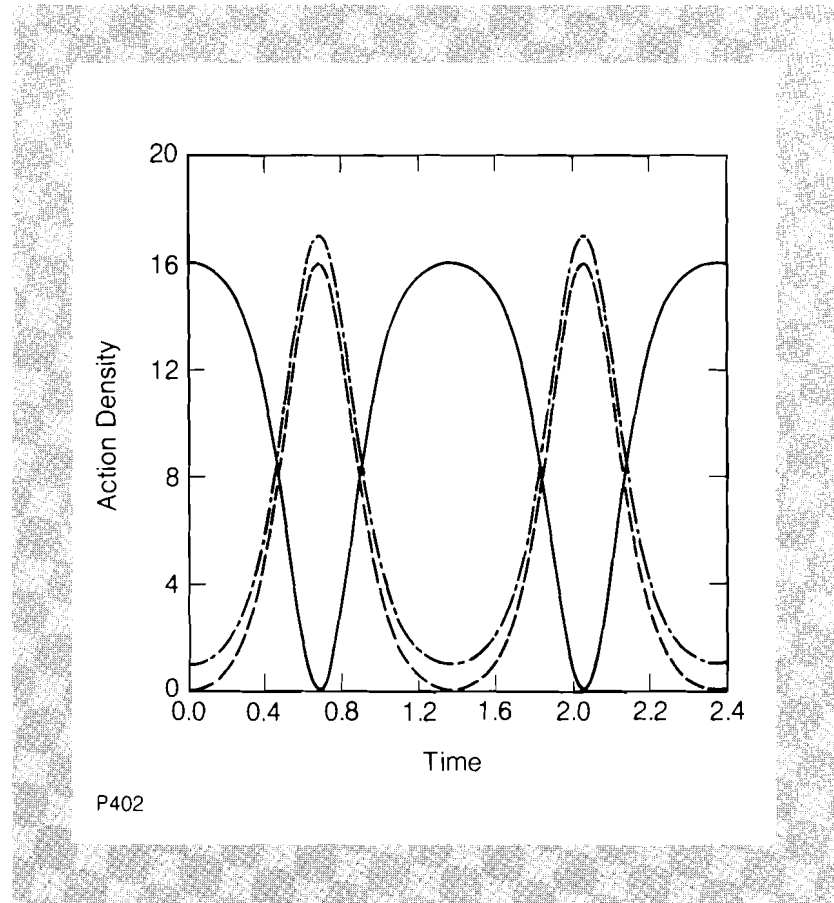
Fig. 23.28
Action density of each mode as a function of time, in units of $mnv_e^2/2\omega_p$. We have taken $v_e/c = 0.040$, $\nu_1 = \nu_2 = \nu_3 = 0$, and set the mismatch ratio equal to zero. The solid line represents mode 1, the dot-dash line represents mode 2, and the broken line represents mode 3.

P402

A more realistic case, however, is to be found in a collisionless plasma where the two electromagnetic waves are undamped and the Langmuir wave is Landau damped. In this case, the governing equations can easily be reduced to a single equation that describes a damped nonlinear oscillator.[5] This is readily solved to determine the temporal behavior of the system. Our results are plotted in Fig. 23.29, in complete agreement with those of Fuchs and Beaudry,[5] and Hiob and Barnard.[6] However, our interpretation differs from that of Hiob and Barnard. During the first half-cycle ($t < 110 \ \Omega^{-1}$), the pump wave transfers action to the daughter waves. In the terminology of quantum field theory, one pump photon decays into a scattered photon and a
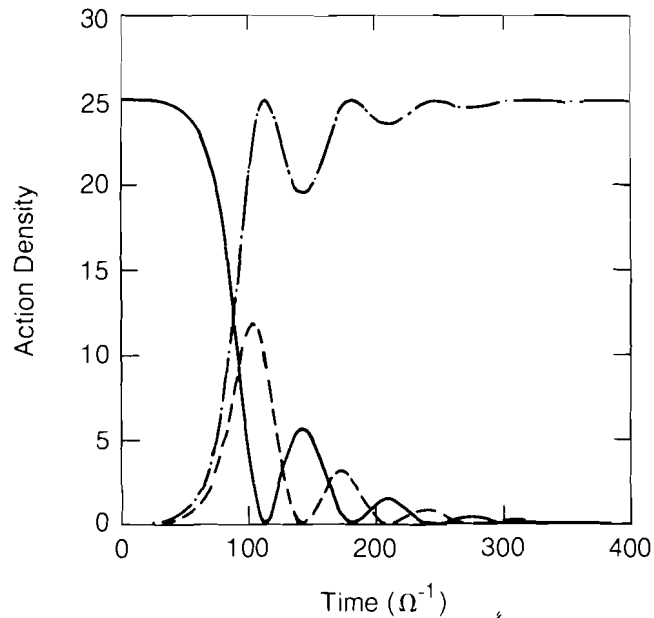
Fig. 23.29
Action density of each mode as a function of time, in units of $mnv_e^2/2\omega_p$. We have taken $v_e/c = 0.040$, $\nu_1 = \nu_2 = 0$, $\nu_3 = 0.020\,\Omega$, and set the mismatch ratio equal to zero. The solid line represents mode 1, the dot-dash line represents mode 2, and the broken line represents mode 3.

P360

plasmon. Because damping acts continually on the plasma wave, at time $t = 110\,\Omega^{-1}$ the action density of the plasma wave is less than that of the scattered electromagnetic wave. Consequently, during the second half-cycle, when a scattered photon and a plasmon recombine to create a pump photon, we run out of plasmons before the action density of the pump can be restored to its initial value. Thus, in each complete cycle, action is irreversibly transferred to the scattered light wave. As time increases, the plasmon action density tends to zero and no recombination can take place. Hence, the system tends to the steady state $E_1 = E_3 = 0$, $E_2 = (\omega_2/\omega_1)\,E_1\,(0)$, as shown in the figure. The steady-state reflectivity, which is defined to be the ratio of the final energy density of mode 2 to the initial energy density of mode 1, is simply

$$R = \omega_2/\omega_1. \tag{4}$$

It is interesting to note that although the time taken to reach the final state depends on ν_3, the reflectivity is independent of it.

The most general case, in which all three waves are damped arbitrarily, occurs in a collisional plasma. It has been shown that a complete analytic solution to this problem cannot be obtained in terms of known functions.[2] However, Eqs. (1a)–(1c) can, of course, be integrated numerically. The result of one such integration is shown in Fig. 23.30. It can be seen that after some transient oscillatory behavior, the system tends asymptotically to a nonlinear steady state. This steady state *can*

be determined analytically. After some algebra, Eqs. (1a)–(1c) yield the following expressions for the action density of each wave:

$$|A_1|^2 = |A_{10}|^2, \tag{5a}$$

$$|A_2|^2 = \frac{\nu_1}{\nu_2} |A_{10}|^2 \left\{ \frac{[m^2 + (m^2-1)r^2]^{1/2} - 1}{(1 + r^2)} \right\}, \tag{5b}$$

$$|A_3|^2 = \frac{\nu_2}{\nu_3} |A_2|^2, \tag{5c}$$

where m is the factor by which the initial pump amplitude exceeds its threshold value [i.e., $A_1(0) = mA_{10}$]. The interpretation of these results is straightforward.
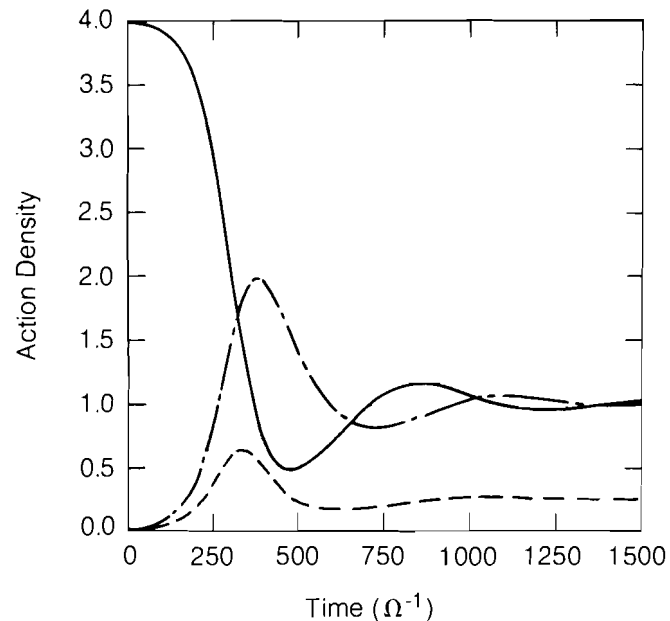
Fig. 23.30
Action density of each mode as a function of time, in units of $mn\nu_e^2/2\omega_p$. We have taken $\nu_e/c = 0.040$, $\nu_1 = \nu_2 = 0.005\,\Omega$, $\nu_3 = 0.020\,\Omega$, and set the mismatch ratio equal to zero. The solid line represents mode 1, the dot-dash line represents mode 2, and the broken line represents mode 3. $I/I_{th} = 4$.

From Eq. (1a), we see that the beating of the two daughter waves gives rise to an electric field at the pump frequency. When δ is equal to zero, the self-generated field is out of phase with the pump field by exactly π radians, so its effect is to decrease the net field at the driving frequency. A nonlinear steady state cannot occur unless the pump amplitude is equal to its threshold value. This determines the strength of the self-generated field, which in turn determines the amplitude of each daughter wave. When δ is nonzero, in addition to being depleted, the pump wave is subject to a nonlinear phase shift that further inhibits the transfer of energy to the daughter waves. In Fig. 23.31 we have plotted the action density of mode 2 as a function of m, for several values of the mismatch ratio.
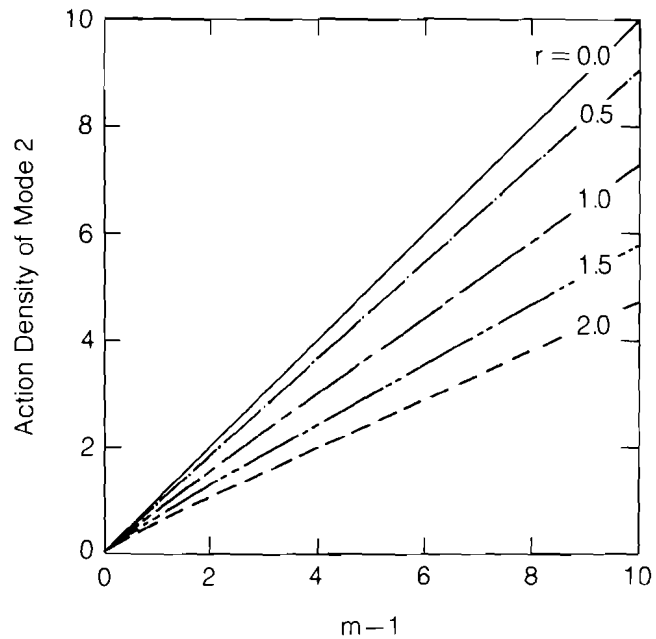
Fig. 23.31
Steady-state action density of mode 2 as a function of m, in multiples of $(\nu_1/\nu_2) |A_{10}|^2$. Results are shown for several values of the mismatch ratio r.

P357

The relationship between the final action densities of modes 2 and 3 is also easily explained. In this three-wave interaction, plasmons and scattered photons are created in pairs. In steady state, the loss of each due to damping must therefore occur at the same rate. Hence $2\nu_2|A_2|^2 = 2\nu_3|A_3|^2$, which is just Eq. (5c).

Rewriting Eq. (5b) in terms of energy densities, we obtain the following expression for the reflection coefficient. This is again defined to be the ratio of the final energy density of the scattered electromagnetic wave to the initial energy density of the pump wave.

$$R = \left(\frac{\omega_2\nu_1}{\omega_1\nu_2}\right) \left\{ \frac{[m^2 + (m^2-1)r^2]^{1/2} - 1}{m^2(1+r^2)} \right\}. \tag{6}$$

This is shown in Fig. 23.32. Notice how the reflection coefficient reaches a maximum, as a function of increasing initial pump intensity, and decreases thereafter. This type of behavior has recently been observed in long-plasma-scale-length experiments performed by Herbst et al.[7] A quantitative comparison of our theoretical predictions with experimental results is now under way.

An important feature of Eq. (6) is its sensitivity to the threshold amplitude of the pump. Thus, any mechanism that alters the threshold can change the steady-state reflectivity. One such mechanism is the breaking of the electron plasma wave, which gives rise to a hot-electron

tail on the electron distribution function. This augments the cold Landau damping by an amount

$$\nu_{Lh} = \left(\frac{\pi}{8}\right)^{1/2} \frac{\omega_p}{(k_3\lambda_D)^2} \frac{n_h}{n_c} \left(\frac{T_c}{T_h}\right)^{3/2} \exp\left[\frac{-1}{2(k_3\lambda_D)^2} \left(\frac{T_c}{T_h}\right) - \frac{3}{2}\left(\frac{T_c}{T_h}\right)\right]. \quad (7)$$

In some cases, ν_{Lh} can be of comparable magnitude to max (ν_{ei}, ν_{Lc}). One must then work with a self-consistent threshold that is itself a function of the incident laser intensity. Offenberger et al.[8] have shown that this can significantly affect the reflectivity. In general, the reflectivity will be reduced.
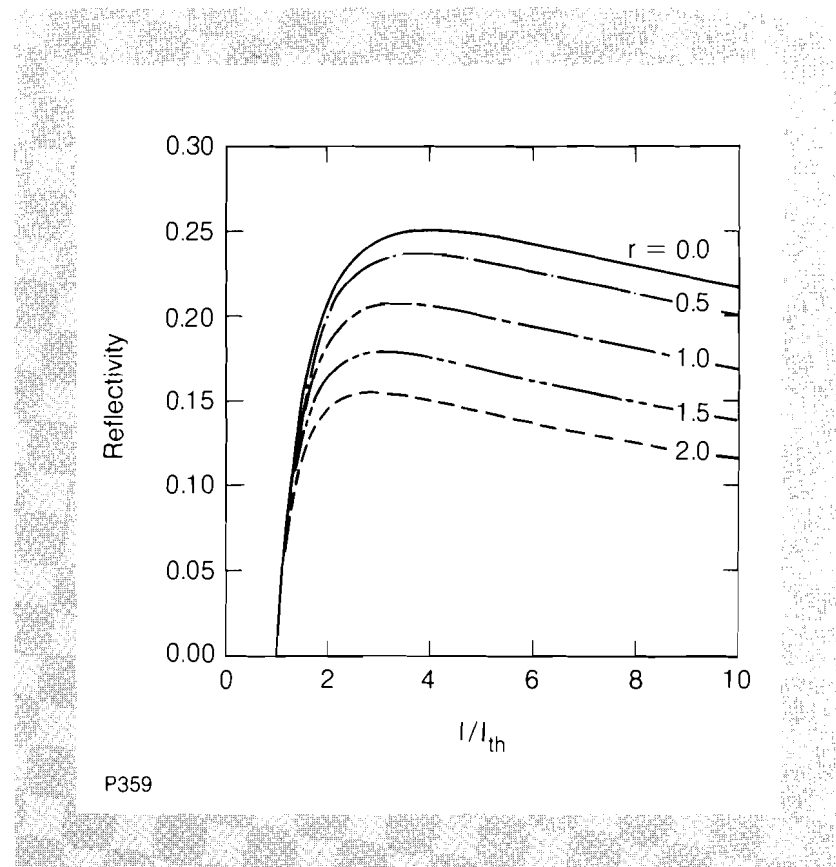
Fig. 23.32
Steady-state reflectivity of the plasma as a function of incident laser intensity, in multiples of $(\omega_2\nu_1/\omega_1\nu_2)$. Results are shown for several values of the mismatch ratio r.

In summary, SRS was considered in a homogeneous plasma, with all three waves damped. The nonlinear saturation of the instability was examined for incident pump amplitudes well in excess of threshold. A nonlinear steady state cannot occur until the pump field is reduced to its threshold amplitude. This determines the magnitude of the self-generated field at the pump frequency, which in turn determines the saturated amplitude of each daughter wave. The resultant reflection coefficient differs from a previous calculation[5] in that it reaches a maximum, as a function of increasing initial pump intensity, and decreases thereafter. This type of behavior has recently been observed in experiments conducted with long-scale-length plasmas.

ACKNOWLEDGMENT

REFERENCES

1. C. J. McKinstrie and A. Simon, LLE Report DOE/DP40124/54 (1984). See also references 1 to 34 contained therein.

2. R. Nakach and H. Wilhelmsson, *Phys. Rev. A* **14**, 451 (1976).

3. C. J. McKinstrie, A. Simon, and E. A. Williams, *Phys. Fluids* **27**, 2738 (1984).

4. R. Z. Sagdeev and A. A. Galeev, *Nonlinear Plasma Theory* (Benjamin, New York, 1969).

5. V. Fuchs and G. Beaudry, *J. Math. Phys. (NY)* **16**, 616 (1975).

6. E. Hiob and A. J. Barnard, *Phys. Fluids* **26**, 3119 (1983).

7. M. J. Herbst *et al., Phys. Rev. Lett.* **52**, 192 (1984).

8. A. A. Offenberger, R. Fedosejevs, W. Tighe, and W. Rozmus, *Physica Scripta* **T2/2**, 498 (1982).

Section 3
ADVANCED TECHNOLOGY DEVELOPMENTS

3.A Measuring Chemically Induced Optical Degradation in Dielectric Thin Films

Plasma-induced etching of dielectric thin films is widely used in integrated-circuit preparation technology. It normally involves the interaction of gas discharge species with a thin-film surface in order to produce volatile reaction products. The ultimate goal is to etch through a film in a spatially selective manner and to thereby generate a desired pattern. This process also occurs unintentionally in the technology related to excimer lasers and fusion reactors. Unintentional etching effects are encountered when dielectric thin films, whose purpose is to establish an optical-interference multilayer stack, are exposed to electrons and ions from the excitation region of excimer gas-lasers. In the same vein, optical coatings that are part of laser-based, nuclear-fuel-reprocessing safeguard monitors and are in direct contact with streams of UF_6 are subject to etching.

While it is not difficult to suspect the performance degradation of a laser or of an optical component following such etching, it is difficult to understand the complexity of physical and chemical surface processes involved in this interaction. In spite of the pioneering efforts by Kay, Winters, Coburn, and Chuang,[1] who systematically ordered etching processes pertinent to plasma-assisted, integrated-circuit etching environments, little is known about the strictly optical consequences of such etching in optical thin films. This report discusses a first attempt to study the optical consequences of dry etching on a simple model system.

This work explores to what extent the absorption (at a certain wavelength) and the thermomechanical properties of a thin film change in response

to a corrosive attack. This information is pivotal if one is to predict the optical damage susceptibility of a thin film when that film becomes part of a high-energy excimer laser cavity and is subject to chemical degradation. Damage of a film is understood here as local, permanent lattice disruption caused by rapid heating and local plasma formation by an incident laser pulse within the film. A prediction of damage susceptiblity must therefore be based on observations of local absorbance, i.e., energy deposition from the laser, and local thermal conductance that is responsible for the rate at which this heat is dissipated. Photothermal displacement spectroscopy is a convenient experimental tool for gathering this information. We present here maps of etched and nonetched thin-film samples, taken by the photothermal displacement method.

The general principles of the photothermal displacement (PTD) technique have been outlined elsewhere.[2] The particular experimental setup used in this work has also been described before.[3] Briefly, an amplitude-modulated 514.5-nm beam (modulation frequency 100 kHz) was focused at normal incidence to a 1.2 (± 0.2)-μm-diameter spot on the film surface by a $60\times$ microscope objective. The same objective also focused a slightly offset, but otherwise collinear, cw He-Ne probe beam next to the green focal spot such that the 632-nm reflection from the film surface was tilted relative to the incident direction whenever the local heating by the green pump beam caused the film surface to expand and form a temporary surface protuberation. This tilt of the reflected red probe beam was monitored by a combination of a position-sensitive detector and two lock-in amplifiers. The tilt-producing slope of the film surface was a product of both the absorbed energy from the pump pulse and the heat conductance of the film. It represented, therefore, an ideal measure for the sought damage susceptibility. Maps of the processed film surface were obtained by stepwise scanning the sample through the pump-probe-foci in x and y directions normal to the beams.

It would clearly be a most definitive experiment that could measure the film changes *in situ* and during the exposure of the film to the chemical agents. However, simple geometrical constraints and other physical limitations make such an endeavor unfeasible. Foremost, the short working distance of a $60\times$ microscope objective shadows large parts of the film surface so that its uniform exposure to a molecular stream of chemical agents cannot be assured. Furthermore, the dielectric surfaces of the objective's refracting elements would fall victim to similar effects as the sample itself, making control of the experiment exceedingly difficult. The data presented here are therefore records of sample conditions measured after the chemical treatment of each sample was completed.

The sample films studied are 1000-Å-thick ThF_4 films that were thermally evaporated onto Au surfaces. (The choice of an Au film as underlying structure is immaterial within the scope of this work. The gold is required for a more extensive investigation into the stability of optical thin films, for which the gold film serves as an inert electrode for measurements to be reported elsewhere.) The gold film rests on a highly polished quartz single-crystal surface. It also is applied by thermal evaporation.

Exposure of the ThF_4-film samples to the chemical and radiation environment typical of an excimer laser discharge region takes place inside a UHV chamber equipped with separate ports and controls for different stimuli. The mixture of simultaneously applied agents comprises XeF_2 as the bearer of the etchant and an electron beam as an irradiation tool. Facilities for simulating ion-impact phenomena are also available, together with standard control instrumentation for residual gas analysis. No ion-impact related effects are, however, reported here.

The irradiation procedure follows a two-stage regimen. First, electron-impact effects are studied in anticipation of optical absorption changes manifesting themselves in photothermal-displacement maps. In order to fully use the imaging capabilities of the PTD technique, the electron-beam dose is increased across the film (at fixed kinetic energy). Samples of the treatment investigated at this point serve as controls for material which goes through the second phase of exposure.

During the second phase, the film is exposed to a stream of molecular XeF_2 at constant flux, in the presence of constant low-energy electron-bombardment. The reasons for this particular choice of stimuli are not based on any optical considerations. The choice is instead motivated by questions of etching-process kinetics and the hope of unraveling chemical reaction-pathways. Nevertheless, for a sample treated in this manner, interesting observations can be made.

The photothermal-displacement map shown in Fig. 23.33 was obtained from a ThF_4-on-gold sample that had experienced both treatment phases in an uninterrupted sequence. For comparison, a background or control map from an identical sample is shown in Fig. 23.34. Both maps are recorded at the same sensitivity and cover the same dynamic range of about one order of magnitude in photothermal-displacement signal. The gray scale in the legend divides this dynamic range into seven equal parts. It must be mentioned here that the very uniform appearance of the control sample, with the exception of the few noticeable polishing scratches, is somewhat deceptive. When ThF_4 samples are withdrawn from the UHV test chamber after irradiation by the 1-keV, 50-μA electron beam, the irradiated region appears blue to the unaided eye. This presumably is caused by halide-vacancy color centers, whose properties in ThF_4 are up to now undocumented in the literature. By merely letting the samples rest at room temperature in ambient laboratory air for a while the coloration fades, indicating diffusion of gas phase constituents into the structural vacancies. As the photothermal displacement apparatus is operated in a standard laboratory setting at a mapping rate of about 8 hours per 200-μm $\times$ 200-μm area, restoration of the sample's initial low optical absorption state is completed before any significant absorption record is assembled.

When electron-damaged ThF_4 is exposed simultaneously to XeF_2 and 1-keV electrons, a different scenario evolves. A restoration of the type shown in Fig. 23.34 does not happen. Even in the absence of added electron bombardment, the incident XeF_2 dissociates at or near the dielectric surface. In this case, the fluorine-depleted surface rapidly

Higher Electron Dose

High ■ Absorption

Low

200 μm

200 μm

G1601

G1602
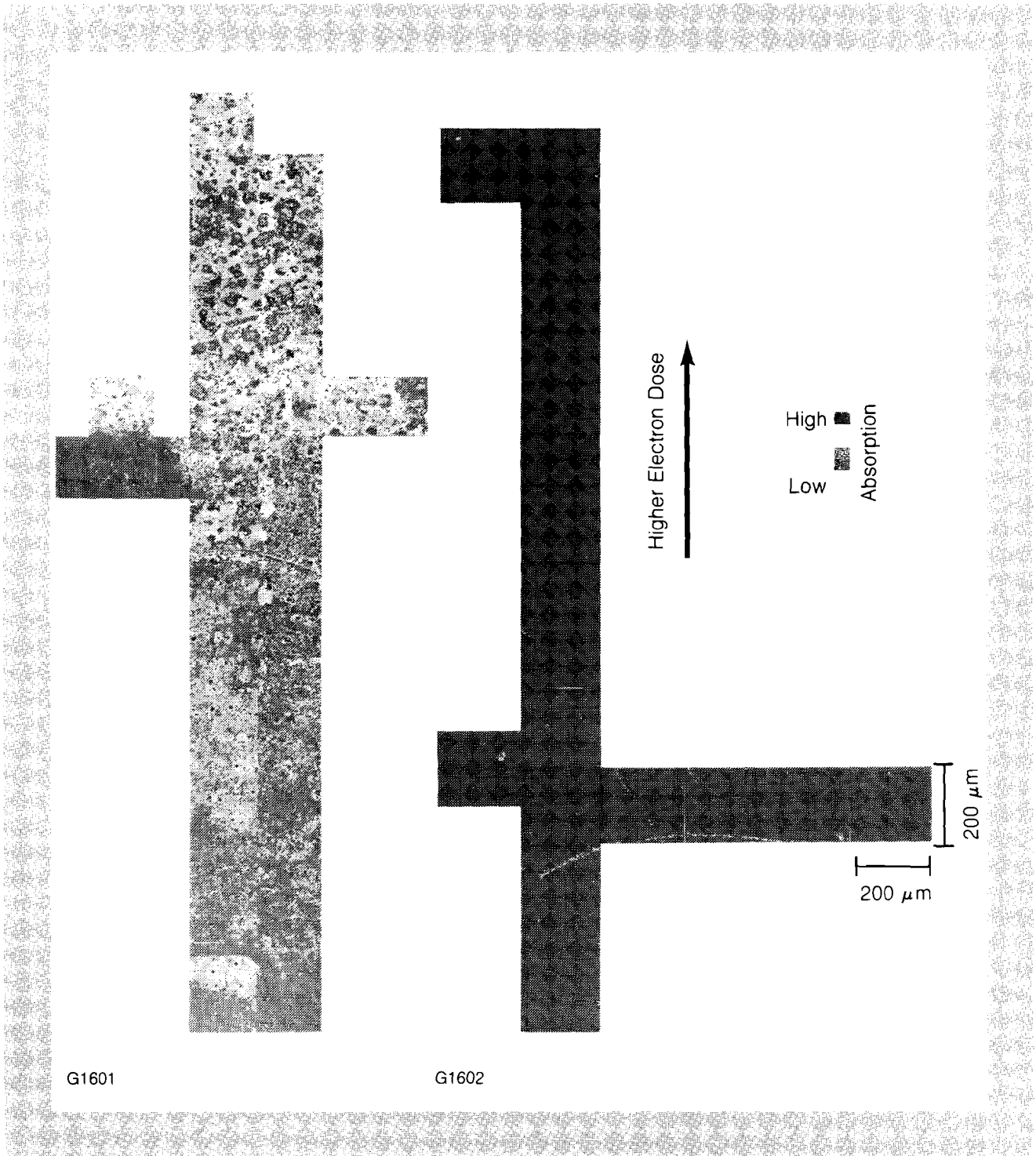
Fig. 23.33
Photothermal-displacement record of
2.5-mm-long strip of 1000-Å ThF₄ thin film
displaying chemically enhanced electron-
induced damage. Total electron dose
varies by a factor of 4 from one end of the
strip to the other.

Fig. 23.34
Photothermal-displacement map of ThF₄
control sample that is similar to sample in
Fig. 23.33 but was not exposed to
chemical agent.

absorbs the equivalent of one monolayer of fluorine; this absorption drops quickly to a rate of one monolayer each seven hours. With the electrons present, two important effects are observed. First, a kinetic-energy-dependent absorption yield is found—i.e., the rate of fluorine uptake per incident electron is energy dependent. This dependence is illustrated in Fig. 23.35, where a resonance-like enhancement near 50 eV becomes apparent. The data in Fig. 23.35 are not deduced optically but by means of microbalance measurements in which the single crystal quartz substrates and the gold electrodes play a key role. Secondly, if uniform co-irradiation by 1-μA, 100-eV electrons is chosen, the fluorine uptake preserves a pattern of the prior, dose-dependent electron-stimulated damage in the film. This is borne out by the photo-thermal displacement map of Fig. 23.33. There, a sample zone is displayed for which all but one of the experimental parameters are kept constant; the 1-keV irradiation dose increases linearly (within experimental accuracy) by a factor of 4 from top to bottom. A highly structured absorption map results.

XeF_2 flux = 1×10^{16} molecules/sec
1000-$\mathring{A}$ ThF_4 film

Permission by: Michael Loudiana, Boeing Aerospace Corp.
G1596
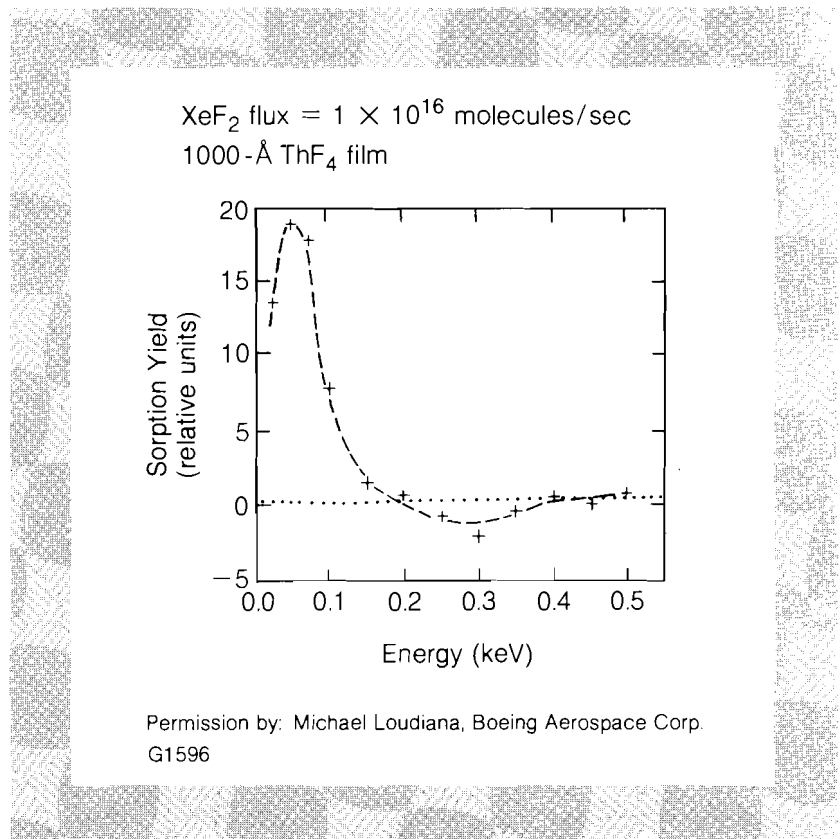
Fig. 23.35
The uptake of fluorine from the XeF_2 stream into the ThF_4 structure is a strong function of the concurrent electron-beam kinetic energy. These data were obtained by Michael Loudiana of Washington State University in samples later analyzed at LLE.

It is essential that during the long experimental runs required for taking such a map, long-term sample changes are investigated. Contrary to the observed rapid filling of absorbing point defects in the control samples by ambient-air constituents, no significant alterations are observed with time for the macroscopic sample appearance or for the microscopic PTD features. The gradual smoothing of the high spatial frequency of strong absorbers from top to bottom of Fig. 23.33, therefore, cannot be attributed to uncontrolled changes in the sample taking hold during PTD scans. An immediate infiltration upon removal of

the treated film from the UHV chamber cannot be ruled out, but it also cannot be accurately measured with existing equipment.

In explaining the clusterlike features of Fig. 23.33, we draw attention to the porous structure of dielectric thin films.[4] Microscopic pores of various throat diameters form during the thin-film growth from the vapor phase, when the component particles arrive at the substrate with thermal kinetic energies. These pores are not unique to the material studied here, nor to the fact that a single layer is being investigated. Pores are known to reach through multilayer thin-film assemblies.[5]

Important effects have been documented for the infiltration of environmental species through these pores.[5] When, for instance, a multilayer, dielectric thin-film stack, which was designed for narrow-band transmission at a certain wavelength, suffered gradual water-vapor invasion through its pores, a frequency shift in the filter's transmission characteristics occurred. By taking advantage of this shift, lateral penetration of water into the stack was imaged in Ref. 5. A pattern of clusters and particles was observed, strikingly similar to the one shown in Fig. 23.33.

Fluid penetration through neutral porous media is controlled by capillary and viscous forces. In the case of dry etching considered here, the etchant does not reach a condensed, fluid state. The driving forces are modified by electrostatic forces arising from charged point defects and defect aggregates in the film lattice. These defects result from the prior electron bombardment of the sample. Their density and absorption cross section at 514 nm are insufficient to cause a significant PTD signal in the control sample (Fig. 23.34). Their formation and aggregation rates in halide crystal lattices are, however, quite dose dependent.[6] It is plausible that an increase in electron dose by a factor of 4 along the strip of Fig. 23.33 produces a significant gradient in the density and spatial frequency of defect clusters. The infiltration pattern of the etchant, and the reaction product formed after infiltration, visually reproduce this condition when monitored by PTD spectroscopy.

These observations have several ramifications for excimer laser systems engineering.

1. The synergism of chemical and physical interaction in fluoride optical thin films is much more deleterious to the film's optical survival strength than each individual effect. This inference can be drawn more forcefully from the microscopic PTD analysis shown here than from traditional thin-film laser-damage experiments.

2. Dose-dependent electron bombardment effects do not "heal" by subsequent, low-energy, continuous irradiation with electrons.

3. The absorption cross section at 514 nm of point defects formed by electron bombardment in ThF_4 is very small.

4. As most fluorides tend to produce stable point defects in the harsh radiation environment typical of excimer laser discharge regions, the findings from ThF_4 can be generalized. Oxides which are less prone to these effects appear to be more favorable thin-film materials for such applications.

ACKNOWLEDGMENT

REFERENCES

1. For a review see J. W. Coburn, "Plasma Etching and Reactive Ion Etching," AVS Monographs Series 1982; and the references therein. H. F. Winters, J. W. Coburn, and T. J. Chuang, *J. Vac. Sci. Technol. B* **1**, 469 (1983).

2. M. A. Olmstead, N. M. Amer, S. Kohn, D. Fournier, and A. C. Boccara, *Appl. Phys. A* **32**, 141 (1983).

3. A. Schmid, D. Smith, M. Guardalben, and J. Abate, in *SPIE Vol. 476 — Excimer Lasers, Their Applications, and New Frontiers in Lasers*, edited by R. W. Waynant (1984), p. 136.

4. H. V. Leamy, G. H. Gilmer, and A. G. Dirks, "The Microstructure of Vapor-Deposited Thin Films," in *Current Topics in Material Science*, edited by E. Kaldis (North-Holland, 1980), Vol. 6.

5. I. Hodgkinson *et al.*, "Structural Effects in Thin-Film Coatings," Technical Digest of Third Topical Meeting in Optical Interference Coatings, Monterey, CA, April 1984.

6. L. W. Hobbs, A. E. Hughes, and J. Pooley, *Proc. R. Soc. London, Ser. A* **332**, 167 (1973).

Section 4
NATIONAL LASER USERS
FACILITY NEWS

This report covers the activities of the National Laser Users Facility for the quarter 1 April to 30 June 1985. During this period five users conducted experiments on LLE facilities. The visiting scientists represented the Lawrence Berkeley Laboratory, Los Alamos National Laboratory, the University of Florida, the University of Maryland, and the University of Texas. The individuals participating in the experiments are listed below.

- **Burton Henke** and **Paul Jaanimagi**
  (Lawrence Berkeley Laboratory)
- **Allan Hauer, James Cobble, William Mead,** and **Phil Goldstone**
  (Los Alamos National Laboratory)
- **C. J. Hooper, Jr.**
  (University of Florida)
- **Hans Griem** and **Samuel Goldsmith**
  (University of Maryland)
- **Carl Collins** and **Suhas Wagal**
  (University of Texas)

The groups from the Lawrence Berkeley Laboratory, the Los Alamos National Laboratory, and the University of Maryland are collaborating on an experiment to study the thermal transport of energy into a hot, laser-produced plasma; the University of Florida is studying spectral line-broadening in dense, laser-produced plasmas; and the University of Texas is studying nuclear fluorescence excited by x rays from a laser-produced

plasma. Each of the groups has accumulated an interesting set of data from their experiments. Further details of these experiments will be presented in future issues of the LLE Review.

As reported in the last issue, the Steering Committee met to review proposals and recommend funding levels to the Department of Energy. Eighteen proposals were submitted to the Steering Committee this year. The proposals were in a variety of areas, including plasma physics, x-ray laser research, x-ray spectroscopy, instrumentation, nuclear fluorescence, materials studies, and others. The committee recommended that ten of these proposals be approved. This year, three new proposals were in this approved category: John Apruzese (Naval Research Laboratory), T.R. Fisher (Lockheed Corporation), and J. Garrett Jernigan (University of California at Berkeley). The individual funding levels for these experiments were recommended to the Department of Energy for their consideration.

The users facility will be accepting proposals until 15 December 1985, the deadline for proposal submission. It is expected that the submission deadline in future years will remain 15 December.

For more information about proposal guidelines and the resources available at the users facility, please contact:

Manager
National Laser Users Facility
Laboratory for Laser Energetics
University of Rochester
250 East River Road
Rochester, New York 14623-1299
(716) 275-2074

ACKNOWLEDGMENT

PUBLICATIONS AND CONFERENCE PRESENTATIONS

Publications

C. Pruitt, "Local Definitions," *Forth Dimensions* **6** (6), 16–17 (1985).

B. Yaakobi, O. Barnouin, J. Delettrez, L. M. Goldman, R. Marjoribanks, R. L. McCrory, M. C. Richardson, and J. M. Soures, "Thermal Transport Measurements in Six-Beam, Ultraviolet Irradiation of Spherical Targets," *J. Appl. Phys.* **57**, 4354–4359 (1985).

T. Norris, T. Sizer II, and G. Mourou, "Generation of 85-fsec Pulses by Synchronous Pumping of a Colliding-Pulse Mode-Locked Dye Laser," *J. Opt. Soc. Am. B* **2**, 613–614 (1985).

I. N. Duling III, T. Norris, T. Sizer II, P. Bado, and G. A. Mourou, "Kilohertz Synchronous Amplification of 85-Femtosecond Optical Pulses," *J. Opt. Soc. Am. B* **2**, 616–618 (1985).

R. Bingham, R. Short, E. Williams, D. Villeneuve, and M. C. Richardson, "The Filamentation Instability at Short Wavelengths," *Plasma Phys. & Controlled Fusion* **26**, 1077–1082 (1984).

M. A. Loudiana, A. Schmid, J. T. Dickinson, and E. J. Ashley, "The Chemical Sputtering of Silicon by Ar^+ Ions and XeF_2," *Surf. Sci.* **141**, 409–416 (1984).

W. Seka, R. W. Short, L. M. Goldman, S. Letzring, M. C. Richardson, J. M. Soures, K. Tanaka, R. S. Craxton, J. Delettrez, R. Boni, and D. Quick, "Half-Integer Harmonic Emission from Laser-Produced Plasmas as a Coronal Temperature Diagnostic," *J. Opt. Soc. Am. B* **1**, 480–481 (1984).

K. Tanaka, B. Boswell, R. S. Craxton, L. M. Goldman, M. C. Richardson, W. Seka, R. W. Short, and J. M. Soures, "Self-Focusing in Underdense Ultraviolet Laser Produced Plasmas," *J. Opt. Soc. Am. B* **1**, 480 (1984).

W. E. Behring, J. F. Seely, S. Goldsmith, L. Cohen, M. Richardson, and U. Feldman, "Transitions of the Type 2s-2p in Highly Ionized Cu, Zn, Ga, and Ge," *J. Opt. Soc. Am. B* **2**, 886–890 (1985).

H. Kim, S. D. Jacobs, and K. A. Cerqua, "Liquid Crystal Laser-Blocking Filters," *Conference Digest, 13th Congress of the International Commission of Optics* (1984), Sapporo, Japan, p. 39 (1985).

F. Guglielmi, "Fabrication of Polymeric Microballoons for Ablative Inertial Fusion Targets," *J. Vac. Sci. Technol. A* **3**, 1274–1276 (1985).

M. C. Richardson, R. S. Craxton, J. Delettrez, R. L. Keck, R. L. McCrory, W. Seka, and J. M. Soures, "Absorption Physics at 351 nm in Spherical Geometry," *Phys. Rev. Lett.* **54**, 1656–1659 (1985).

D. R. Dykaar, T. Y. Hsiang, and G. A. Mourou, "An Application of Picosecond Electro-Optic Sampling to Superconducting Electronics," *IEEE Trans. Magn.* **21**, 230–233 (1985).

T. G. Dziura and D. G. Hall, "Semiclassical Theory of Bistable Semiconductor Lasers including Radial Mode Variation," *Phys. Rev. A* **31**, 1551–1557 (1985).

N. D. Delamater, C. F. Hooper, Jr., R. F. Joyce, L. A. Woltz, N. M. Ceglio, R. L. Kauffman, R. W. Lee, and M. C. Richardson, "Opacity Effects on Hydrogenlike X-Ray Lines Emitted from Laser-Driven Implosions," *Phys. Rev. A* **31**, 2460-2463 (1985).

H. Kim and M. D. Wittman, "X-Ray Microradiography of Inertial Fusion Targets Using a Laser Produced Plasma as an X-Ray Source," *J. Vac. Sci. Technol. A* **3**, 1262–1265 (1985).

S. G. Noyes and H. Kim, "Aluminum/Aluminum Nitride Sputter Deposition on the Inertial Fusion Target Using the Pulsed Gas Process," *J. Vac. Sci. Technol. A* **3**, 1201–1203 (1985).

F. Guglielmi, "Low Density Foam for Self-Focusing Inertial Fusion Targets," *J. Vac. Sci. Technol. A* **3**, 1208–1209 (1985).

B. A. Brinker, "Microradiographic Self-Imaging of DT Filled Laser Fusion Targets," *J. Vac. Sci Technol. A* **3**, 1269 (1985).

R. L. Schriever, J. L. Emmett, R. L. McCrory, D. Giovanielli, S. Bodner, and G. Yonas, *J. Fusion Energy* **4**, 115–128 (1985).

K. E. Meyer and G. A. Mourou, "Two-Dimensional E-Field Mapping with Subpicosecond Temporal Resolution," *Electron. Lett.* **21**, 568–569 (1985).

Forthcoming Publications

U. Feldman, J. F. Seeley, M C. Richardson, W. E. Behring, and S. Goldsmith, "Transitions of the Type 2s-2p in Fluorine-Like and Oxygen-Like As, Se, Br and Rb^x," to be published in the *Journal of the Optical Society of America B*.

P. Horn, P. Braunlich, and A. Schmid, "Photoacoustic Determination of Three-Photon Absorption Cross Sections in Thallium Halides at 1.06 μm," to be published in the *Journal of the Optical Society of America B*.

C. J. McKinstrie and A. Simon, "Nonlinear Saturation of Stimulated Raman Scattering in a Collisional Homogeneous Plasma," to be published in *Physics of Fluids*.

W. Seka, B. B. Afeyan, R. Boni, L. M. Goldman, R. W. Short, K. Tanaka, and T. W. Johnston, "Diagnostic Value of Odd-Integer Half-Harmonic Emission from Laser-Produced Plasmas," to be published in *Physics of Fluids*.

K. A. Tanaka, B. Boswell, R. S. Craxton, L. M. Goldman, F. Guglielmi, W. Seka, R. W. Short, and J. M. Soures, "Brillouin Scattering, Two-Plasmon Decay, and Self-Focusing in Underdense UV Laser-Produced Plasmas," to be published in *Physics of Fluids*.

S. Williamson, G. Mourou, and J. C. M. Li, "Time-Resolved Laser-Induced Phase Transformation in Aluminum," to be published in the *Proceedings of MRS Symposium on Energy Beam-Solid Interactions and Transient Thermal Processing*.

J. F. Seeley, C. M. Brown, U. Feldman, M. Richardson, B. Yaakobi, and W. E. Behring, "Evidence for Lasing on the 182-Å Transition of CVI in a Radiation-Cooled Plasma," to be published in *Optics Communications*.

G. Albrecht, M. Grunersen, and D. Smith, "An Active Mode-Locked Q-Switched Oscillator Using Nd^{3+} Doped Glass as the Active Medium," to be published in the *IEEE Journal of Quantum Electronics*.

P. Bado and M. Bouvier, "A Multikilohertz Pockels Cell Driver," to be published in *Review of Scientific Instruments*.

W. A. Lampeter, "Computerized Search of Chest Radiographs for Tumors," to be published in *Investigative Radiology*.

W. A. Lampeter, "ANDS-VI Computer Detection of Lung Nodules," to be published in the *Proceedings of Medical Imaging and Instrumentation 1985, Society of Photographic Scientists and Engineers*.

B. Yaakobi, R. D. Frankel, J. M. Forsyth, and J. M. Soures, "Laser Generated X-Ray Source for Time-Resolved Biological and Material Structure Studies," to be published in the *Proceedings of a Symposium on New Methods in X-Ray Absorption, Scattering, and Diffraction*.

R. L. McCrory, O. Barnouin, R. S. Craxton, J. Delettrez, R. Epstein, L. Forsley, L. M. Goldman, R. J. Hutchison, R. L. Keck, H. Kim, W. Lampeter, S. A. Letzring, R. S. Marjoribanks, P. McKenty, M. C. Richardson, W. Seka, R. W. Short, A Simon, S. Skupsky, J. M. Soures, K. Swartz, K. Tanaka, C. Verdon, and B. Yaakobi, "Short-Wavelength,

Direct-Drive Laser Fusion Experiments at the Laboratory for Laser Energetics," to be published in *Plasma Physics and Controlled Nuclear Fusion Research 1984* (IAEA, Vienna).

D. P. Butler, T. Y. Hsiang, and G. A. Mourou, "Transient Relaxation of the Normal State Resistance of Tin Microstrips in the Presence of Current Bias," to be published in the *Journal of Low Temperature Physics*.

Conference Presentations

S. Jacobs, "Liquid Crystal Devices for Laser Systems," presented at the Technical Symposium: "Lasers and Particle Beams for Fusion and Strategic Defense," Rochester, NY, April 1985 (invited talk).

The following presentations were made at the Gamma-Ray Laser Workshop, Institute for Defense Analysis, Alexandria, VA, May 1985:

S. Letzring, B. Yaakobi, and M. C. Richardson, "Diagnostics for Gamma-Ray Laser Candidate Measurement" (invited talk).

B. Yaakobi, S. Letzring, J. M. Soures, F. Marshall, and M. C. Richardson, "Properties of X-Rays from UV-Laser-Irradiated Targets Relevant to Pumping Nuclear Transitions" (invited talk).

The following presentations were made at the Conference on Lasers and Electro-Optics '85, Baltimore, MD, May 1985:

R. S. Marjoribanks, M. C. Richardson, O. Barnouin, B. Yaakobi, R. L. Keck, S. A. Letzring, G. Stradling, S. R. Goldman, P. D. Goldstone, A. Hauer, and W. C. Mead, "Spectral and Temporal Characteristics of X-Ray Emission from UV-Irradiated Spherical High-Z Targets."

K. E. Meyer, D. R. Dykaar, and G. Mourou, "Two-Dimensional E-Field Mapping and High-Speed Device Characterization Using the Electro-Optic Sampling Technique."

G. Mourou and S. Williamson, "Picosecond Electron Probe for Direct Investigation of Lattice Temperature and Structural Phase" (invited talk).

T. Norris, I. N. Duling III, M. Pessot, T. Sizer II, J. Dawes, and G. A. Mourou, "Generation of Microjoule, 65-fs Pulses at High Repetition Rate."

M. C. Richardson, W. Beich, J. Delettrez, M. Dunn, L. Folnsbee, R. J. Hutchison, S. A. Jacobs, R. Keck, T. Kessler, W. Lampeter, R. Leary, S. Letzring, F. J. Marshall, R. L. McCrory, S. Morse, R. Peck, G. Pien, C. Pruitt, D. Quick, F. Rister, W. Seka, M. Simpson, S. Skupsky, D. Smith, J. M. Soures, C. P. Verdon, W. Watson, and D. Whiteman, "OMEGA — A 24-Beam UV Irradiation Facility" (invited talk).

B. Yaakobi, "Thermal Transport in Laser-Irradiated Targets," and "X-Ray Measurement Techniques in Laser Fusion and X-Ray Laser Studies," presented at the Spring College on Radiation in Plasmas, Trieste, Italy, May 1985 (invited talks).

W. R. Donaldson and G. A. Mourou, "Improved Contacts on Intrinsic Silicon for High Voltage Photoconductive Switching," presented at the 5th IEEE Pulsed Power Conference, Arlington, VA, June 1985.

S. Williamson, G. Mourou, and J. C. M. Li, "Genesis of Melting," presented at the Rochester Condensed Matter Symposium, Department of Physics and Astronomy, University of Rochester, Rochester, NY, June 1985.

W. A. Lampeter, "Computerized Search of Chest Radiographs for Nodules," presented at Computer-Assisted Radiology, Berlin, West Germany, June 1985.

K. E. Meyer, D. R. Dykaar, and G. A. Mourou, "Characteristics of TEGFET's and MESFET's Using the Electro-Optic Sampling Technique," presented at the Device Research Conference, Boulder, CO, June 1985.

The following presentations were made at the 1985 Rochester Forth Conference, Rochester, NY, June 1985:

G. Ball, R. Boni, and W. Seka, "Computerized Pulse Train Diagnostics for Kuizenga Oscillators."

L. P. Forsley, "nth-Order Defining Words."

The following presentations were made at the Workshop on the Physics of Laser Fusion, Vancouver, B. C., June 1985:

J. Delettrez, "Thermal Electron Transport in Direct-Drive ICF."

L. M. Goldman, "The Use of Laser Harmonic Spectroscopy as a Target Diagnostic."

A. Simon, "Raman Scattering."

The following presentations were made at the 15th Annual Anomalous Absorption Conference, Banff, Alberta, Canada, June 1985:

O. Barnouin, J. Delettrez, L. M. Goldman, R. Marjoribanks, M. C. Richardson, J. M. Soures, and B. Yaakobi, "Thermal Transport Measurements in 24-Beam, UV Irradiation of Spherical Targets."

J. Delettrez, P. A. Jaanimagi, B. L. Henke, and M. C. Richardson, "Temporal Dependence of the Mass Ablation Rate in UV-Laser-Irradiated Spherical Targets."

R. Epstein, J. Delettrez, M. C. Richardson, and B. Yaakobi, "Numerical Simulation and Target Design for Laser-Imploded Cylindrical Plasmas."

P. A. Holstein, J. Delettrez, K. Swartz, S. Skupsky, and J. P. Matte, "Study of Delocalized Heat Flux with and without Hydrodynamics."

F. J. Marshall, M. C. Richardson, P. Jaanimagi, R. L. Keck, H. Kim, S. A. Letzring, R. S. Marjoribanks, R. L. McCrory, P. McKenty, J. M. Soures, and C. P. Verdon, "Multibeam, UV-Irradiated High-Aspect-Ratio Targets."

F. J. Marshall and M. C. Richardson, "Uniformity of X-Ray Flux from Gold-Coated Spherical Targets."

C. J. McKinstrie and A. Simon, "The Absolute Stimulated Raman Scattering Instability in a Finite Collisional Plasma."

M. C. Richardson, O. Barnouin, P. Jaanimagi, R. L. Keck, H. Kim, S. A. Letzring, R. J. Marshall, R. L. McCrory, P. McKenty, J. M. Soures, C. P. Verdon, and B. Yaakobi, "Ablative Fusion Targets Driven by the 24-Beam UV OMEGA System."

M. C. Richardson, O. Barnouin, R. Epstein, P. A. Jaanimagi, R. S. Marjoribanks, J. M. Soures, and B. Yaakobi, "Laser-Imploded Cylindrical Plasmas."

M. C. Richardson, R. L. Hutchison, R. L. Keck, H. Kim, S. A. Letzring, F. J. Marshall, R. L. McCrory, P. McKenty, J. M. Soures, and C. P. Verdon, "24-Beam, 2-kJ Implosion Experiments with OMEGA."

W. Seka, L. M. Goldman, A. Simon, F. J. Marshall, and M. C. Richardson, "Raman Scattering in Laser-Produced Plasmas."

R. W. Short, "The Weibel Instability Driven by Hot Electrons in the Plasma Corona."

A. Simon, R. W. Short, W. Seka, and L. M. Goldman, "Enhanced Thomson Scattering Theory Applied to Eight Experiments."

K. Swartz, R. W. Short, and A. Simon, "The Effect of Multiple Beams on Parametric Instabilities."